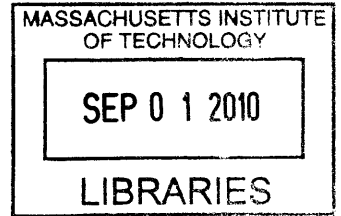


# Carbon-Based Electric Double Layer Capacitors for Water Desalination

by

Batya A. Fellman



Submitted to the Department of Mechanical Engineering  
in partial fulfillment of the requirements for the degree of

Masters of Science in Mechanical Engineering

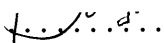
**ARCHIVES**

at the

MASSACHUSETTS INSTITUTE OF TECHNOLOGY

June 2010

© Massachusetts Institute of Technology 2010. All rights reserved.

Author .....  .....

Department of Mechanical Engineering

May 19, 2010

Certified by ...  .....

Evelyn N. Wang

Assistant Professor of Mechanical Engineering

Thesis Supervisor

Accepted by .....  .....

David E. Hardt

Professor of Mechanical Engineering

Chairman, Graduate Thesis Committee

# Carbon-Based Electric Double Layer Capacitors for Water Desalination

by

Batya A. Fellman

Submitted to the Department of Mechanical Engineering  
on May 19, 2010, in partial fulfillment of the  
requirements for the degree of  
Masters of Science in Mechanical Engineering

## Abstract

In capacitive deionization (CDI), salt water is passed through two polarized electrodes, whereby salt is adsorbed onto the electrode surface and removed from the water stream. This approach has received renewed interest for water desalination due to the development of new high-surface area, carbon-based nanomaterials. However, there is limited understanding as to how electrode geometry, surface properties, and capacitance affect ion capture. In this work, we experimentally investigated various standard carbon-based electrode materials, including activated carbon and carbon cloths, as well as microfabricated silicon structures for CDI. Electrochemical characterization through cyclic voltammetry was used to determine the electrochemical properties of each material. The capacitance values of the carbon materials tested were 40 F/g for 2000 m<sup>2</sup>/g carbon cloth, 32 F/g for 1000 m<sup>2</sup>/g carbon cloth, and 25 F/g for activated carbon. In addition, we constructed two iterations of flow test channels to perform parametric studies on ion capture. The first flow cell utilized a commercial conductivity probe to measure salt concentration after charging the electrodes without flow. We showed that the ion capture on both the carbon cloth and activated carbon electrodes were proportional to the applied voltage, however two orders of magnitude smaller than what is expected from the electrode charge. We addressed a significant experimental limitation in the second flow cell by integrating conductivity sensors into the flow channel to measure effluent salt concentration during electrode charging. We found that the salt adsorption increased from 33.1  $\mu\text{mol/g}$  in the first flow cell to 63.5  $\mu\text{mol/g}$  in the redesigned flow for an applied potential of 1.2 V. Future directions will focus on controlling electrode geometry and chemistry to help elucidate transport mechanisms and provide insight into the design of optimal materials for capacitive deionization.

Thesis Supervisor: Evelyn N. Wang  
Title: Assistant Professor of Mechanical Engineering

## Acknowledgments

The author gratefully acknowledges the help and support of Professor Evelyn Wang whose ideas and guidance were instrumental in completing this work. Additionally the author would like to acknowledge the members of the Device Research Lab, especially Dr. Ryan Enright, Tom Humprik, and Jeremy Cho, for their useful discussions and advice throughout this work; the staff and all those associated with the Microsystems Technology Laboratories at the Massachusetts Institute of Technology, who provided guidance in developing the processes and recipes to produce the devices used in this study; and Professor Yang Shao-Horn and the Electrochemical Energy Lab for use of their equipment for the electrochemical measurements. The author would also like to thank the King Fahd University of Petroleum and Minerals in Dhahran, Saudi Arabia, for funding the reported research through the Center for Clean Water and Clean Energy at MIT and KFUPM and for funding through the National Science Foundation Graduate Fellowship.

# Contents

<b>1</b>	<b>Introduction</b>	<b>6</b>
<b>2</b>	<b>Literature Review</b>	<b>11</b>
<b>3</b>	<b>Theoretical Aspects of Electrokinetics in Capacitive Deionization</b>	<b>15</b>
3.1	Physical Basis of the Electric Double Layer . . . . .	15
3.2	Electrokinetics at Large Applied Voltages . . . . .	19
3.3	Porous Electrodes . . . . .	22
<b>4</b>	<b>Electrochemical Characterization</b>	<b>26</b>
4.1	Basic Testing Techniques . . . . .	26
4.1.1	Cyclic Voltammetry . . . . .	27
4.1.2	Chronocoulometry . . . . .	28
4.2	Carbon-Based Materials . . . . .	28
4.2.1	Material Morphology . . . . .	28
4.2.2	Electrochemical Characterization . . . . .	29
4.3	Silicon Microstructures . . . . .	34
4.3.1	Nanopillars Fabrication . . . . .	35
4.3.2	Nanopillars Electrochemical Characterization . . . . .	36

<b>5</b>	<b>Initial Flow Cell Experiments</b>	<b>38</b>
5.1	Design . . . . .	38
5.2	Experimental Setup and Instrumentation . . . . .	39
5.3	Results and Discussion . . . . .	41
<b>6</b>	<b>Microfabricated Flow Cell Redesign</b>	<b>49</b>
6.1	Concept and Design . . . . .	50
6.1.1	Conductivity Sensors . . . . .	51
6.2	Device Fabrication . . . . .	53
6.3	Experimental Setup . . . . .	55
6.4	Results and Discussion . . . . .	56
6.5	Measurement Challenges . . . . .	60
<b>7</b>	<b>Summary and Future Directions</b>	<b>63</b>
7.1	Future Directions . . . . .	64
7.1.1	Carbon Electrode Study Redesign . . . . .	64
7.1.2	Controlled Geometries . . . . .	65
7.1.3	Electrokinetics near a Flat Plate . . . . .	66
	<b>References</b>	<b>68</b>
<b>A</b>	<b>Literature Review Summary Chart</b>	<b>73</b>
<b>B</b>	<b>Fabrication Process Flow</b>	<b>75</b>
<b>C</b>	<b>Matlab Scripts</b>	<b>77</b>
C.1	Flow Cell Real-Time Concentration Calculation . . . . .	77
C.2	Micro Flow Cell Data Analysis . . . . .	78

# Chapter 1

## Introduction

Clean water can no longer be considered a forsaken resource in both the developing and developed worlds. With increasing population growth and industrial demands, water is becoming one of our most valuable and scarce commodities. Of the Earth's water capacity, 97.5% is currently non-potable as saltwater. Of the 2.5% which is fresh water, only 0.3% is a renewable source of clean water with the remainder locked in ice caps and other nonrenewable sources [1]. Since 1.2 billion people in the world today lack access to fresh drinking water, with that number expected to grow dramatically within the next 20 years, being able to capture just a small fraction of the 97.5% salt water by desalination could greatly help to mitigate our ensuing water crisis [2].

Reverse osmosis and multi-stage flash are the current leading desalination technologies. Multi-stage flash is a thermal-based desalination technology whereby fluid enters chambers with successively lower temperatures and pressures to vaporize the water in the feed solution then condensing the pure water as seen in Figure 1-1. Because it is a thermal process relying on phase change, it is highly energy intensive requiring over 1000 kWh/m<sup>3</sup> of energy [3].

Reverse osmosis is a membrane based separation process. By applying a pressure exceeding the osmotic pressure of 27 bar (generally twice the osmotic pressure around 54 bar),

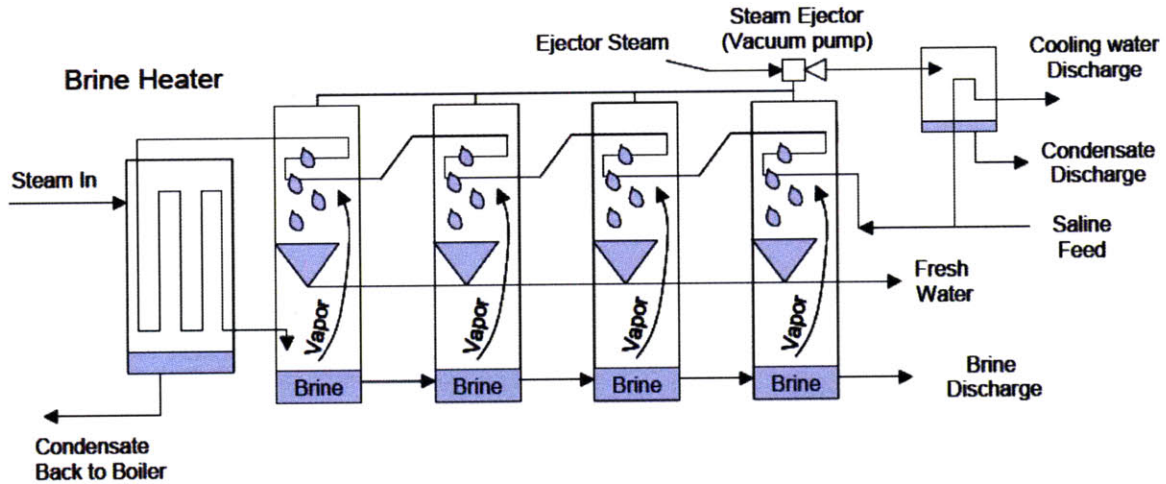


Figure 1-1: Multi-stage flash is a thermal-based desalination technology whereby fluid enters chambers with successively lower temperatures and pressures to vaporize the water in the feed solution then condensing the pure water. Figure adapted from [1].

water is forced to flow against the osmotic gradient through a semi-permeable membrane as seen in Figure 1-2. The past 20 years have seen a great improvement in the energy efficiency of reverse osmosis through the use of pressure recovery systems. Today, reverse osmosis plants are capable of producing clean drinking water at an energy requirement of less than  $12 \text{ kWh/m}^3$ , while the theoretical minimum is  $1.29 \text{ kWh/m}^3$  at 75% recovery and are therefore the dominant desalination technology in the United States [2].

Even with these high energetic efficiencies, reverse osmosis is not without challenges. The large pressures needed to desalt seawater require reverse osmosis plants to have a large footprint and high capital costs. Furthermore, biofouling is one the primary operating challenges for reverse osmosis plants by greatly decreasing membrane permeability over time. Chemical pretreatments are used to mitigate the membrane fouling by removing some organic material, however it persists as dominant issue. Due to these restrictions, there is still a need for a competitive technology that can operate in smaller, portable units with lower pressures. Capacitive deionization (CDI) can fill that need.

Capacitive deionization is a water purification technique achieved by the electrosorption

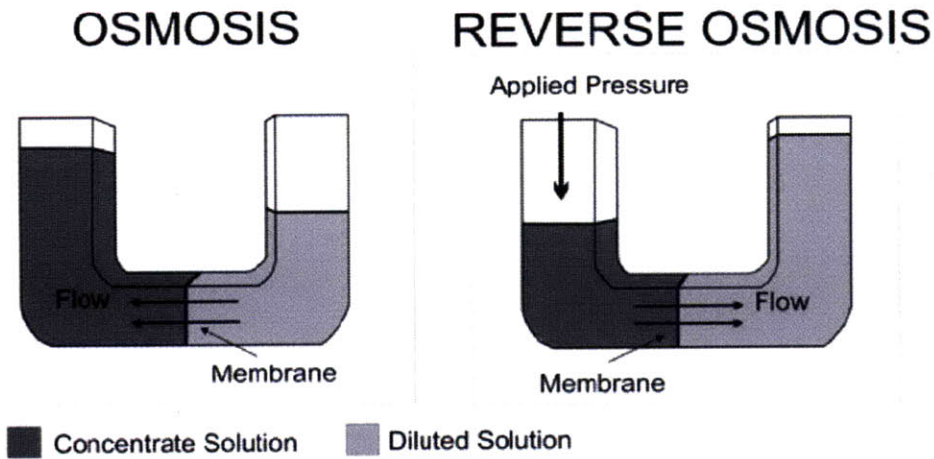


Figure 1-2: Reverse osmosis is a membrane-based separation process where a pressure exceeding the osmotic pressure is applied to the solution to force water to flow against the osmotic pressure gradient. Figure adapted from [4].

of ions onto porous electrodes. Water passes through charged electrodes, causing the ions to electromigrate and adsorb on the electrode surface to shield the surface charge, as shown in Figure 1-3. This process subsequently reduces the concentration of the outlet stream. When the ions are in this charged state, energy is stored analogous to an electric double layer capacitor. By releasing the ions from the electric double layer into a purge stream, this energy can be reclaimed and the electrode surfaces can be cleaned for future adsorption cycles. Because this technique charges and discharges a series of electrochemical capacitors in a cycle, the theoretical efficiency should be very high, especially for lower concentrations of feed solution such as brackish water. As the feed solution concentration increases, the energy required to desalt the water increases due to the finite adsorption capacity of the electrodes. For that reason, CDI focuses on brackish water instead of more concentrated seawater, which is one of the major limitations compared to reverse osmosis and multi-stage flash.

Although macroscopically CDI appears to be relatively straight-forward, the ion transport locally within the electrode is not well understood. The modeling of CDI is challenging due



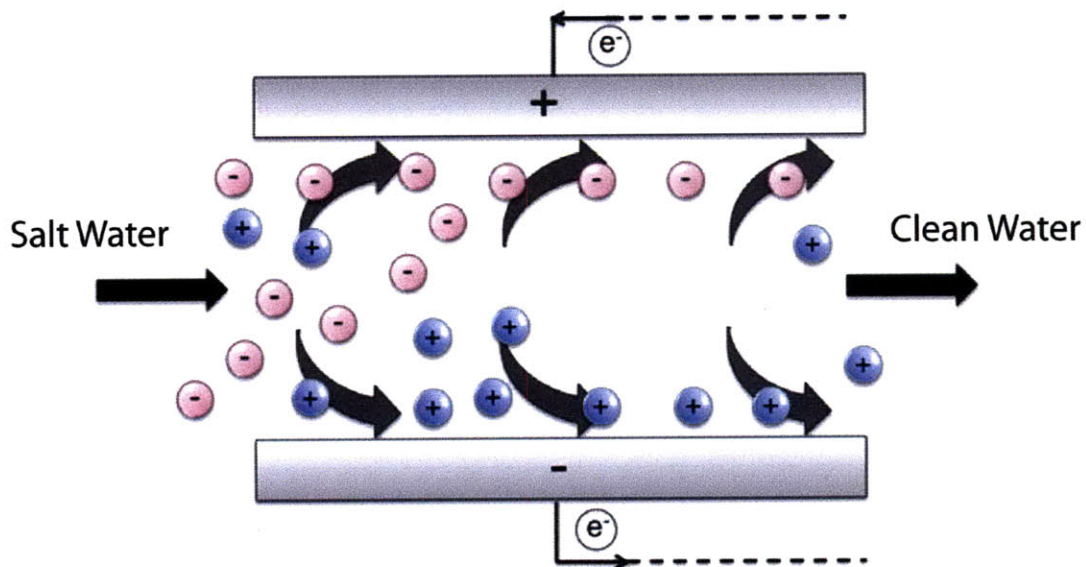


Figure 1-3: Schematic of capacitive deionization showing salt water flowing between two electrodes. By charging the electrodes, the ions adsorb onto the surface, thereby reducing the concentration of the output water stream.

to large applied surface potentials of around 1 V, long charging times, complicated electrode geometry, and small, confined pore spaces where linear electrokinetic theory does not apply. Aside from a few studies, most of the research has been experimental and focuses on novel electrode synthesis, especially modifications to standard carbon-based materials. Most of these carbons, such as activated carbon and carbon cloth, contain tortuous and non-uniform pores that further complicate the ion transport. The ability to understand ion transport within nanometers of the electrode-electrolyte interface can greatly enhance the ability to tailor materials to ease transport into the pores. On the macroscopic level, this manifests itself as enhanced efficiency in electrosorptive materials, which can help make CDI a more marketable desalination technology.

In this study, we initiated understanding of ion capture on electrode materials for CDI. We first examine the scope of the previous literature highlighting major progress and short-

comings in Chapter 2. Subsequently, we address the theoretical aspects of electrokinetics in CDI, as well as the challenges for modeling the electrosorption process in Chapter 3, prompting us to examine the problem experimentally. In Chapter 4, we investigated the electrochemical behavior of commercially available activated carbon and carbon cloth when applied as an aqueous capacitor as well as controlled nano- and microfabricated silicon structures. In Chapters 5 and 6, we examined the carbon materials ability to absorb salt in two mini-channel flow experiments. The first flow cell experiment in Chapter 5, had a clear diffusion limitation during the charging and focuses on steady state behavior of the electrodes, while the redesigned flow channel addressed in Chapter 6 eliminates the primary diffusion limitation by convectively replenishing the bulk concentration and monitoring the transient ion capture in the system. We finally address in Chapter 7 the need for further experiments to better understand the fundamental physics of capacitive deionization.

# Chapter 2

## Literature Review

Although capacitive deionization (CDI) was first investigated in the 1960s and 1970s [5], it reemerged in the 1990s with Farmer and coworkers employing carbon aerogel electrodes with surface areas ranging from 400-1000 m<sup>2</sup>/g [6–8]. They demonstrated that with the proper high-surface area material, CDI can energetically compete with existing desalination technologies such as reverse osmosis. Most of the research since Farmer has focused on finding new high specific surface area materials that can enhance CDI. Since CDI is another application of an electrochemical capacitor, the materials that are investigated tend to follow the state-of-the-art in the supercapacitor community [9]. Recently, studies have explored the capacitive behavior of activated carbon, activated carbon cloth, and carbon nanotubes (CNTs) [10–15]. These materials, especially the activated carbon derivatives, inherently have large specific surface areas on the order of 1000-2000 m<sup>2</sup>/g due to the large volume of micro and mesopores with characteristic diameters of 2-10 nm.

With activated carbon based electrodes, one major challenge for water desalination is the hydrophobicity of the electrode material, which is a challenge unique to CDI. Supercapacitors tend to focus on nonaqueous electrolytes so the capacitors can charge to higher voltages of 4-6 V and are not limited to the standard 1.23 V for the electrolysis of water as given by

the Nernst equation for pH of 7 at 25°C. The electrode hydrophobicity is especially critical for activated carbon electrodes where a hydrophobic polytetrafluoroethylene(PTFE) binder is required to maintain the material consistency. Lee *et al.* investigated this limitation by adding ion-exchange resin to a standard activated carbon and PTFE slurry to increase the electrode hydrophilicity and observed 35% enhancement in performance [16].

Furthermore, various surface modifications show promise for increasing the electrosorption of salt. Oh *et al.* demonstrated that the efficiency of activated carbon cloths could also be improved through surface modification with a nitric acid (HNO<sub>3</sub>) solution which increases the presence of carboxyl, carbonyl, and hydroxyl functional groups on the carbon surface, aiding in the absorption [12]. They further concluded that the surface carbonyl groups added by the HNO<sub>3</sub> modification increased the efficiency not only through double layer electrosorption but also through electron transfer by Faradaic reactions to remove inorganic salts. Additionally, modification of activated carbon cloths through incorporation of titania (TiO<sub>2</sub>) also demonstrated an increase in electrosorption capability [15]. The titania inclusions increased the total electrosorption of salt by a about factor of three from 70  $\mu\text{mol/g}$  to 230  $\mu\text{mol/g}$ , which is attributed to the increase in adsorption strength from the titania. There are also various reports of effective ion capture using carbon nanotube and nanofiber (CNT-CNF) composite electrodes fabricated by chemical vapor deposition. It is suggested that the CNT-CNF electrodes have a morphological advantage over standard activated carbon by having a larger fraction of mesopores (2-50 nm) than micropores (less than 2 nm) as in the activated carbon. Although the specific surface area is smaller than the activated carbon as measured by nitrogen absorption in a BET test (210  $\text{m}^2/\text{g}$  compared to 1500  $\text{m}^2/\text{g}$ ) [17], the larger presence of the mesopores reduces the effect of overlapping double layers which are especially prevalent at the sub-2 nm range and hinder transport of ions into the pores by effectively reducing the accessible pore diameter [13, 18, 19]. Ultimately even though the surface area is an order of magnitude smaller for the CNT-CNF electrodes

the electrooptive capacity is  $56.8 \mu\text{mol/g}$  compared to  $83 \mu\text{mol/g}$  as reported for activated carbon cloth.

The microstructure of the electrode material, as suggested by the CNT-CNF studies, may prove to have a significant effect on both the electrochemical characterization and the electrosorption. Li *et al.* demonstrated with ordered mesoporous carbons (BET surface area ranging from  $1000 \text{ m}^2/\text{g}$  to  $1500 \text{ m}^2/\text{g}$ ) that even given a larger capacitance value, a material may underperform for ion capture [20]. Although the mechanism is unclear, this phenomenon was attributed to a more ordered structure aiding the transport. The fabricated ordered mesoporous carbons (OMC) had pore distributions that are more uniform and ordered than their activated carbon counterparts. The OMCs varied by the type of nickel salt included in the synthesis. They investigated three main types of OMCs: OMC-S with the inclusion of nickel sulfate hexahydrate, OMC-N with nickel nitrate hexahydrate, and OMC-W without any nickel. The pore size distribution was centered around 3-4 nm for all of the OMCs, which is well above the hydrated ion size of about 0.7 nm for sodium [21, 22], but the OMC-W did have a slightly large mean pore size of 4 nm compared to 3.3 nm in the OMC-N and 3.7 nm in OMC-S. The discrepancy between the higher capacitance of the OMC-N sample over the OMC-W sample while exhibiting a lower amount of salt adsorption was attributed to a more ordered pore structure in the OMC-W aiding in ion transport, although both OMCs outperformed the activated carbon sample in both capacitance and ion capture. This anomaly between the electrochemical characterization and electrosorption indicates that further understanding of the basic physics governing the CDI process is needed in order to design materials to optimize the system efficiency.

Aside from a few studies [23–25], most of the research so far for CDI has been experimental, focusing on novel electrode synthesis, especially modifications to standard carbon-based materials. However there exists a lack of continuity across the literature in regards to testing procedures and parameters. Appendix A shows a table highlighting the majority of the liter-

ature on capacitive deionization. Among the studies, there exists a variety of concentrations tested ranging from less than 1 mM to over 0.1 M as well as a range of voltages below 1.5 V. However, because each study tends to choose its own set of parameters, it is difficult to accurately compare different studies as well as glean insight into the underlying physics where the theory is still under development. Because of the lack of continuity in the literature, we decided to take a more systematic approach to investigating ion capture in CDI. Instead of focusing on material modifications, we chose to probe existing state-of-the-art materials while altering system parameters to eventually map out the parameter space and understand how ion capture changes with such variables as concentration and applied voltage.

Additionally, there is also limited understanding of the transport phenomena at the electrode-electrolyte interface that can subsequently be used to tailor advanced materials for more efficient CDI. This is in part due to the complex nature of the charging process arising from large applied voltages and complex electrode geometries. By focusing on how a single material is affected by a variety of parameters, we can experimentally elucidate the underlying physics. As theoretical models start to evolve to more realistically capture system behavior, research is beginning to shift its focus to understanding material performance in the context of these theoretical considerations [26].

## Chapter 3

# Theoretical Aspects of Electrokinetics in Capacitive Deionization

### 3.1 Physical Basis of the Electric Double Layer

When most surfaces are placed in contact with an aqueous solution, the surface acquires surface charge. This surface charge can be attributed to a variety of phenomena but most commonly charge dissociation and specific adsorption of ions. The surface charge will affect the distribution of ions within close vicinity of the interface. Counter-ions of opposite charge to the surface will be attracted, while co-ions will be feel a repulsive force. The resulting distribution of ions near the surface is distinct from the electroneutrality prescribed in the bulk and is termed the electric double layer (EDL). The net charge in the EDL is exactly equal and opposite to the charge exhibited by the surface. The net concentration of counter- and co-ions allows a potential distribution to develop near the surface which decays to a zero potential outside the EDL in the bulk solution. Figure 3-1 illustrates conceptually how the ions arrange near a charged surface and the resulting potential distribution that develops. A more complete description of the composition of the EDL will be addressed later in this

chapter.

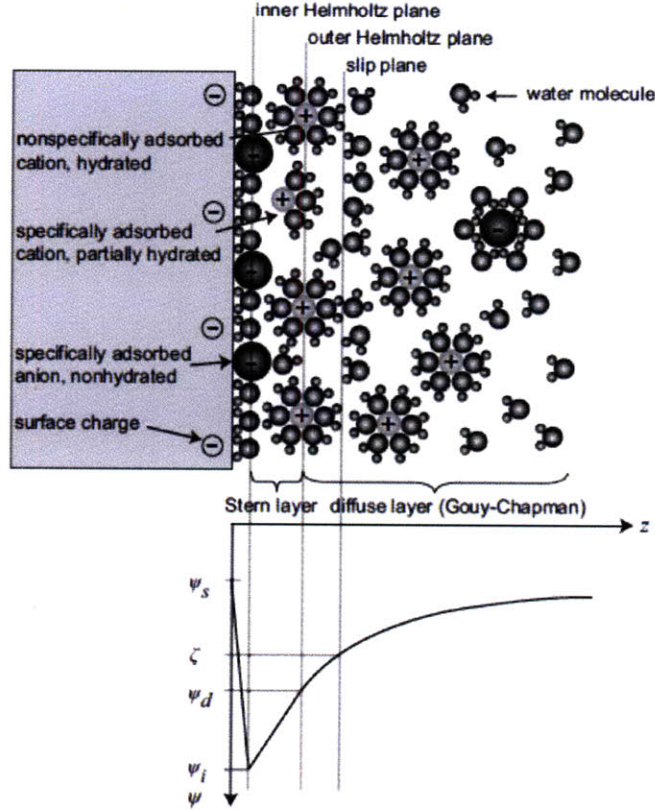


Figure 3-1: The electric double layer is classically composed of two distinct regions: the inner Sten layer and the outer diffuse layer. Figure adapted from [27].

A basic expression for the concentration and potential distributions near a surface can be obtained by starting with the definition of the electrochemical potential of the  $i^{th}$  species  $\mu_i$ ,

$$\mu_i = \mu_i^0 + kT \ln \frac{\rho_i}{\rho^0} + z_i e \phi, \quad (3.1)$$

where  $\mu^0$  is the standard potential,  $\rho^0$  is the number density in the bulk,  $\rho_i$  is the number density of species  $i$ ,  $z_i$  is the valence number on species  $i$ ,  $\phi$  is the potential,  $e$  is the charge on an electron,  $k$  is the Boltzmann constant, and  $T$  is the temperature. For equilibrium to hold, the gradient of the electrochemical potential must be equal to zero. From this condition the Boltzmann distribution is derived giving a relation for the ionic concentration as a function



of the special potential:

$$c_{\pm} = c_0 \exp\left(\frac{\mp zF\phi}{RT}\right), \quad (3.2)$$

where  $c$  is the local concentration,  $c_0$  is the concentration in the bulk,  $F$  is Faraday's constant and equal to the charge in a mole of electrons, and  $R$  is the universal gas constant. Furthermore, Maxwells equation relates the electric potential  $\phi$  to the spacial charge distribution  $\rho_E$  by:

$$\nabla^2\phi = \frac{\rho_E}{\epsilon}, \quad (3.3)$$

where  $\epsilon$  is the permittivity and the spatial charge distribution is defined as

$$\rho_E = F \sum z_i c_i. \quad (3.4)$$

Combining the above equations yields a differential equation allowing one to solve for the electrical potential in space and therefore obtain the concentration distribution given by

$$\frac{d^2\phi}{dx^2} = \frac{2zFc_0}{\epsilon} \sinh\left(\frac{zF\phi}{RT}\right). \quad (3.5)$$

Typical boundary conditions used set the potential  $\phi$  as a specified potential  $\phi_w$  at the wall at  $x = 0$  and  $\phi = 0$  as  $x$  tends to infinity, *e. g.* electrically neutral in the bulk.

A common approximation for the Poisson-Boltzmann equation, Eqn. 3.5, is the Debye-Huckel approximation and assumes that the voltage is small relative to the thermal voltage  $kT/e$  or similarly  $RT/F$  of 25.7 mV at 25°C. Eqn. 3.5 can then be reduced to

$$\frac{d^2\phi}{dx^2} = \frac{\phi}{\lambda_D^2} \quad (3.6)$$

defining the Debye length  $\lambda_D$  as

$$\lambda_D = \left( \frac{\epsilon RT}{2F^2 z^2 c} \right)^{1/2}. \quad (3.7)$$

This result can then be integrated with the boundary conditions  $\phi = \phi_w$  at  $x = 0$  and  $\phi = 0$  as  $x$  tends to infinity for a flat plate geometry to obtain a simplified potential distribution of

$$\phi = \phi_w \exp\left(-\frac{x}{\lambda_D}\right). \quad (3.8)$$

The characteristic length scale  $\lambda_D$  defined in Eqn. 3.7 represents an effective decay length and is known as the Debye length. For an symmetrical aqueous electrolyte at room temperature this reduces to

$$\lambda_D = \frac{3.04 \times 10^{-10}}{(z^2 c)^{1/2}} \quad (3.9)$$

by substituting the appropriate constants  $R$  and  $F$  and the permittivity of water  $\epsilon$ . Typical values for the Debye length ranges from less than a nanometer for 1 M 1:1 electrolyte to about 10 nm for a 1 mM solution. Since the Debye length is essentially a decay length, at distance of three times  $\lambda_D$  away from the surface, the potential has decayed to 5% of its original value.

Concentration ( $z = 1$ ) (mM)	Debye length $\lambda_D$ (nm)
$10^3$	0.3
$10^2$	1
10	3
1	10

Table 3.1: The Debye length as a function of concentration for a monovalent electrolyte in an aqueous solution.

## 3.2 Electrokinetics at Large Applied Voltages

The above analysis, modeling the ions as point charges, is known as the Gouy-Chapman theory [28]. Gouy-Chapman considered the electric double to be merely a diffuse layer of ions near the surface; however if a moderate surface potential of for example 250 mV, about 10 times the thermal voltage, is applied to the Poisson-Boltzmann distribution, this implies that the concentration of counter-ions near the surface is  $e^{10}$  or  $22 \times 10^3$  times the bulk concentration. This result is well beyond the maximum packing limit of about 5,000 mol/m<sup>3</sup>, modeling the ions as spheres with diameter of 0.7 nm, even for a 1 mM bulk solution. This unphysical increase in the concentration is due to the fact that the ions are modeled as point charges in the Gouy-Chapman analysis. In fact, the ions are of finite size and cannot be simply modeled as point charges. Stern first addressed this issue by modeling the double layer as multiple regions. Near the surface exists what is known as the Stern layer, and consisting of an adsorbed layer of ions with a potential drop denoted as  $\Delta\phi_S$ . Outside of this layer is the diffuse layer where the concentration is assumed to be small enough to model the ions as point charges where the remainder of the potential drop  $\Delta\phi_D$  occurs. The composition of the electrical double layer is shown in Figure 3-1 [27]. Separating the inner Stern layer from the outer diffuse layer is what is termed the outer Helmholtz plane. At this interface, the electrical potential is termed the zeta potential, and is the surface potential can be measured experimentally using Phase Analysis Light Scattering. It should also be noted that hydrodynamic slip is actually assumed to occur at the outer Helmholtz plane which is important for electroosmotic flow.

The addition of the Stern layer adds a quick fix for some of the invalid assumptions of the Gouy-Chapman theory. In reality the ions have a fixed size including a hydration shell which further increases the effective ion size in an aqueous medium. A standard sodium ion has a radius of 0.3 nm with a hydrated ion size 0.7 nm [21]. Additional theory has been recently

developed to provide a more complete model for the electric double layer that includes the steric effects. By defining a maximum packing concentration of the ions, Bazant *et al.* re-addressed the formation of the electric double layer under large applied voltages. From the Boltzmann distribution in equation 3.2, we can rearrange it to define a maximum potential  $\phi_c$  when the concentration of the electrolyte with ion size  $a$  has reached the packing limit:

$$\phi_c = -\frac{RT}{zF} \ln(a^3 c_0) = \frac{RT}{zF} \ln\left(\frac{c_{max}}{c_0}\right) \quad (3.10)$$

Classical double layer theory can still be applied even through the weakly nonlinear regime of less than about 13 times the thermal voltage since the steric effects are not apparent in the diffuse layer and dilute solution theory can still hold, although linear approximations are invalid. Figure 3-2 illustrates how these steric effects change the structure of the double layer compared to the point charges in the Gouy-Chapman theory [29].

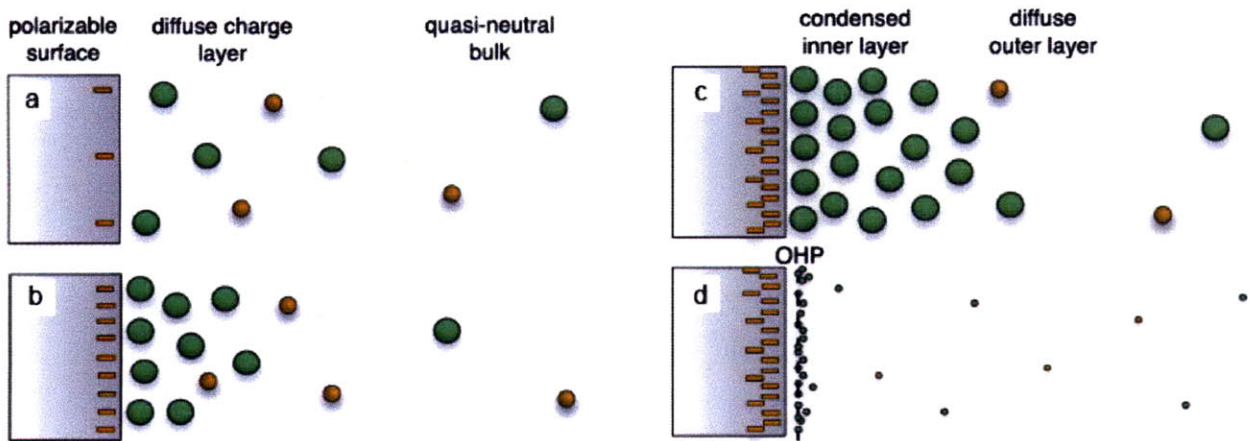


Figure 3-2: General Gouy-Chapman theory (d) does not account for the steric effects arising from finite ion size. At low voltages and concentrations, this theory is valid, but at high voltages the steric effects must be accounted for. As the surface is progressively charged (a-c) more counter-ions migrate towards the surface and arrange themselves with some minimum distance between adjacent ions. This packing effectively increases the size of the double layer beyond the standard Debye length. Figure adapted from [29].

The consequence of the finite ionic size ultimately changes the distribution of ions and concentration near the surface as well as the subsequent double layer capacitance. Figure 3-3 shows how this concentration is affected. The dotted line is the standard Poisson-Boltzmann theory modeling the atoms as point charges whereas the solid lines show the modified Poisson-Boltzmann accounting for steric effects. As the potential in the diffuse layer increases (note that this is not the applied surface potential since that is still assumed to be reduced by the Stern layer voltage), the length of the double layer is extended to account for the finite packing size. Although standard Poisson-Boltzmann theory provides a fair approximation for small voltages, at the large voltages required for capacitance charging for both supercapacitors and capacitive deionization, there are additional physical effects that must be accounted for that are missing from the classical theory.

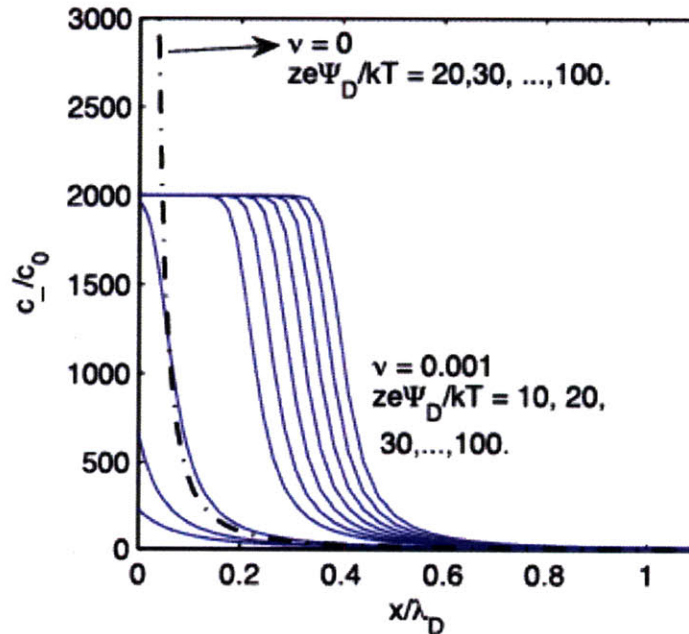


Figure 3-3: The concentration near a surface as a function of distance is shown for increasing voltages. The dotted line illustrates the distribution for standard Poisson-Boltzmann theory where ionic size is not an issue, while the solid line shows the modified theory accounting for steric effects. As the voltage increases, the ions reach a maximum packing concentration which cannot be exceeded thereby modifying the concentration of ions near the surface. Figure adapted from [29].

### 3.3 Porous Electrodes

With the correction for steric effects introduced into the modified Poisson-Boltzmann equation, a more accurate representation of the ion distribution near a surface for large voltages can be obtained. However, actual electrodes used in supercapacitors and for capacitive deionization cannot simply be modeled as a flat plate or other simple model geometries. The high surface area in these electrodes comes from an intricate network of microscopic pores. These pores are generally a few nanometers in diameter. At this scale, not only is it possible for overlapping double layers to exist in the pores complicating the electrokinetics, but there may also exist further transport limitations due to diffusion.

The analysis for the electric double layer documented above accounts for the steady state behavior. With porous electrodes, the transient behavior during charging and discharging become increasingly important due to limits of diffusion slowing the transport of ions into the electrode. A full model for the charging process must couple the Nernst-Planck equation for the transport of ions into the electrode with the Poisson-Boltzmann equation for how the ions interact with each other and the surface depending on the potential. Additionally, in capacitive deionization, because the water is flowing through the system, ideally the Navier-Stokes equation is also used to determine how the fluid in the system moves and how the ions in the double layer are affected by the applied flow. To actually solve the full problem is numerically intensive and has not yet been attempted.

Recent work has addressed the diffusional coupling with the salt adsorption and capacitive charging [23]. To make the model tractable, the standard Gouy-Chapman-Stern theory was used without account for any additional steric effects at the large voltages modeling the ions as point charges. Also, instead of solving the Nernst-Planck equation for transport in the entire system, a stagnant diffusion layer was assumed to occur just outside the electrode surface such that ions in that layer are affected both by a diffusional concentration gradient

and electromigration due to a voltage gradient. The authors identified two main regimes during the charging process: the capacitive charging regime for short time scales or low applied voltages where the transport behavior is weakly nonlinear and the strongly nonlinear desalination regime for long time scales or large applied voltages. The two regimes are demonstrated in Figure 3-4 [23]. In the weakly nonlinear regime, the capacitor charges both by expelling co-ions from the diffuse part of the double layer as well as adsorbing counter-ions. For longer times (or large applied voltages) in the strongly nonlinear, desalination regime, the capacitive charging is mainly due to the adsorption of counter-ions as the co-ions have primarily been expelled from the double layer. It is this desalination regime that the bulk concentration is significantly altered and depleted of salt. It is important to note that the idea that surface charge shielding in the EDL occurs both due to counter-ion adsorption and co-ion repulsion. This necessitates that the ion capture by the electrode will be a fraction of the actual applied surface charge, which is an important consequence in CDI systems [24, 26, 30].

The work discussed above highlights the progress that has been made to better understand the physics of ion transport in porous electrodes. However, because of the complex geometries of electrodes used in real systems and the difficulty in accurately modeling the entire capacitive deionization process, most researchers have taken an experimental approach to investigating CDI. The recent theoretical advancements highlight the importance of understanding how changes in concentration and applied voltage affect the ion capture in the EDL. Overall, the existing literature has yet to probe the physics by systematically changing these parameters and have instead focused purely on material modifications. Without understanding how a material's electrosorptive capacity changes both with changes in voltages and concentration, it is difficult to isolate changes that occur purely from material modifications. The opportunity exists to bridge this gap in understanding by experimentally examining the parameter space to increase understanding of the physics involved in the elec-

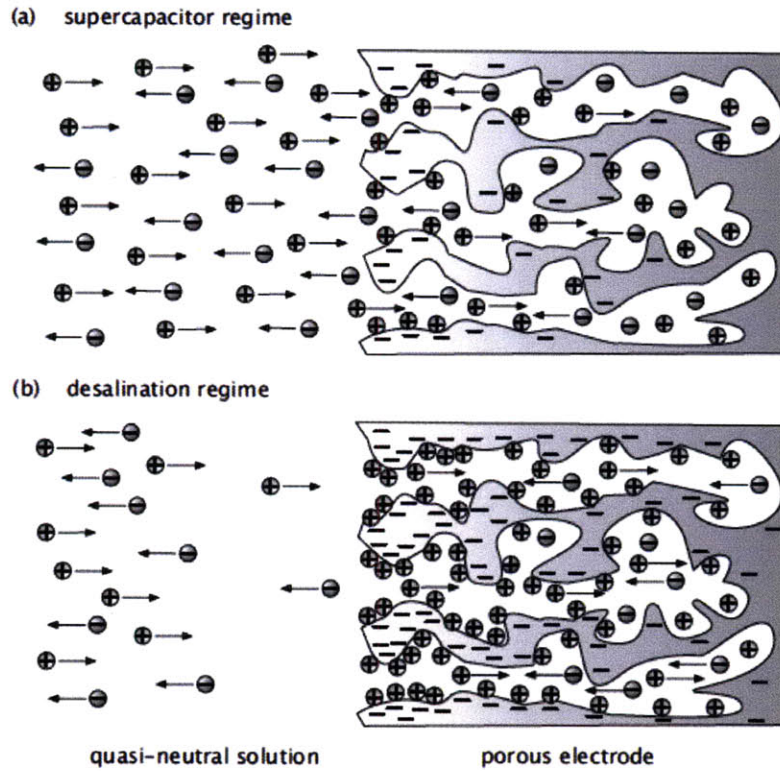


Figure 3-4: During capacitor charging there are two main regimes. (a) For short time scales or low applied voltages the transport behavior is weakly nonlinear and is denoted the capacitor regime, while (b) for long time scales or large applied voltages the transport is strongly nonlinear and denoted as the desalination regime. Figure adapted from [23].



adsorption process. Eventually, comparing experimental results to the proposed theory can determine how well the recent theoretical advancements in electrokinetics at large voltages match the actual physical process. To initiate bridging this divide, we decided to take an experimental approach to capacitor charging and ion capture in the EDL. By performing both electrochemical measurements and ion capture measurements in a flow channel, we can begin to understand how ion accumulation in the EDL during capacitive charging relates to ion capture in CDI under various conditions.

# Chapter 4

## Electrochemical Characterization

The first step in beginning to understand the electrosorption of ions in capacitive deionization is to perform standardized electrochemical testing to characterize the capacitance of different materials. Although from previous work it is clear that there is no direct correlation between the capacitance and electrosorption capability of a material [20], it can serve as an initial indicator for a material's performance. In this chapter we first outline the basic electrochemical methods used to measure the capacitance. We then apply these techniques to two different classes of materials: amorphous, carbon-based electrodes and controlled, microfabricated silicon structures.

### 4.1 Basic Testing Techniques

Testing for electrochemical characterizations is standardly performed on a potentiostat. A potentiostat is capable of controlling the voltage difference across a working electrode and a counter electrode with the aid of a reference electrode. The reference electrode such as the standard hydrogen electrode, saturated calomel electrode, or silver-silver chloride electrode is always at a constant potential. This allows the potentiostat to independently control

the voltage drop between the reference and the working electrode as well as the reference and counter electrode by using a series of op amps. For electrochemical characterizations where reduction or oxidation reactions are not the focus, a two electrode setup will suffice where a standard reference electrode is not used. In that case the relative potential between the two electrodes is controlled. In general potentiostats are used for the electrochemical characterizations because they allow for precise control over cell voltage as well as a dynamic range of potential sweeps [31].

### 4.1.1 Cyclic Voltammetry

The primary method used to characterize capacitor properties is cyclic voltammetry (CV). Cyclic voltammetry sweeps through a range of voltages using a linear ramp rate, and the current response as a function of time is monitored. The resulting current is plotted as a function of the voltage. Since the charge  $Q$  on a capacitor is defined by

$$Q = CV \tag{4.1}$$

with capacitance  $C$  and voltage  $V$ , it follows that time derivative of charge is the current  $I$  is given by

$$I = C \frac{dV}{dt}. \tag{4.2}$$

For an ideal electric double layer capacitor with a constant capacitance, the current response should be constant since the scan rate is constant. For capacitors where Faradaic reactions occur, a peak in the current response is measured at the voltage associated with the charge transfer. Aside from obtaining the average capacitance value of a material, the shape of the CV diagram can elucidate the charging behavior of a material with a specific electrolyte. For example, if a CV test was performed on a pure resistor, the current response would simply be linear since  $V = IR$ . Deviations from the ideal CV diagram can qualitatively indicate if

an electrochemical capacitor exhibits a large resistance by observing if the current response is linear with respect to the voltage instead of constant with increasing voltage.

### **4.1.2 Chronocoulometry**

Chronocoulometry, like cyclic voltammetry, is another technique for probing the capacitance of a material. A step voltage is applied to the electrodes and the resulting current response is monitored. The charge accumulation over time can then be extracted by integrating the current response. Chronocoulometry is a more direct approach for measuring material capacitance than cyclic voltammetry and provides different insight into the dynamical behavior of the system. By analyzing the charge on the electrode over time, charging timescales can be extracted. These charging timescales can subsequently be examined to provide insight into whether diffusion limitations exist, therefore hindering the capacitive charging.

## **4.2 Carbon-Based Materials**

The first set of electrodes we chose to examine were carbon-based materials, specifically activated carbon and activated carbon cloth. Carbon electrode materials are often used in the supercapacitor industry due to the high conductivity and high specific surface area of the electrodes. These properties also make the materials ideal candidates for testing in capacitive deionization applications.

### **4.2.1 Material Morphology**

Activated carbons and activated carbon cloth materials tend to have specific surface areas in the range of 1000 m<sup>2</sup>/g to 2000 m<sup>2</sup>/g. This large surface area is due to the multi-scale effects of the activation process. Figures 4-1(a) and 4-1(b) show SEM images of commercially

available activated carbon cloth and activated carbon. Although the visible features in the image are all micron-sized, these materials also exhibit a high density of non-uniform, tortuous pores that range in size from 2 to 10 nm. These pores account for most of the increase in specific surface area. For testing in the flow cell, we acquired activated carbon cloth samples from American Kynol. The samples varied in surface area, having a specific surface area of either 1000 m<sup>2</sup>/g or 2000 m<sup>2</sup>/g. We also obtained activated carbon samples from Maxwell Technologies, for use in commercially available supercapacitors for additional comparison.

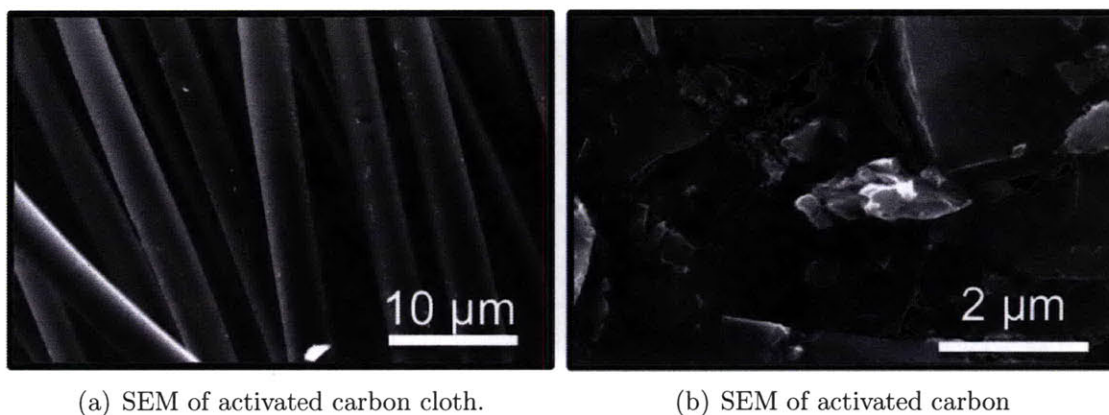


Figure 4-1: Both of the SEMs show activated carbon in a different form. Although, the structure varies on the micro-scale, beyond the resolution of the SEM exist a vast network of sub-2 nm pores accounting for the large increase in specific surface area.

#### 4.2.2 Electrochemical Characterization

Various electrochemical testing was carried out on the activated carbon and carbon cloth materials. Cyclic voltammetry using a potentiostat (model 1470E, Solartron Analytical) was used to characterize the electrical capacitance of each material. A 1 M NaCl electrolyte was used with Celgard 5401 aqueous-specific polypropylene separators. The scans were performed at sweep rates of 10 mV/s and 50 mV/s. Figure 4-2 shows the CV diagram for 2000 m<sup>2</sup>/g at the different sweep rates. Although the sweep rate changes the shape of the curve, the

measured capacitance value does not change. From the change in shape of the CV curve between the 10 mV/s and 50 mV/s scan rates, we speculate that a transport limitation evolves. At each successive voltage step, the current has to keep increasing to get a sufficient number of ions to the electrode to shield the charge and becomes increasingly difficult. This transport limitation is a direct consequence of the large surface area. For that reason we will compare the subsequent materials at a lower scan rate of 10 mV/s.

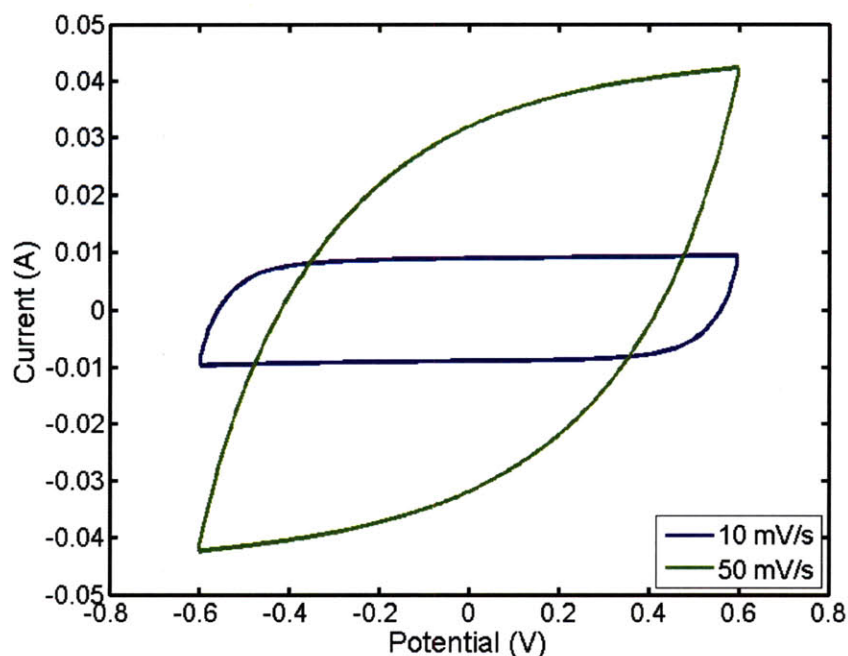


Figure 4-2: Cyclic voltammograms of the 2000 m<sup>2</sup>/g carbon cloth at sweep rates of 10 mV/s and 50 mV/s. Even though the current response varies for the different scan rates, the average capacitance value remains constant.

The resulting CV diagrams comparing the two different surface area carbon cloths and activated carbon at the lower scan rate of 10 mV/s can be seen in Figure 4-3. From the CV diagrams, an average capacitance value for the electrode materials was determined. The largest surface area carbon cloth at 2000 m<sup>2</sup>/g had the highest specific capacitance of 40 F/g, followed by the lower surface area carbon cloth at 32 F/g, and the activated carbon had the lowest capacitance of 25 F/g. The capacitance results are summarized in Table

4.1. The activated carbon electrodes, however, exhibited a large degree of hydrophobicity compared to the carbon cloth due to the presence of a hydrophobic PTFE binder. The contact angle was not specifically measured for this material, but reports in the literature place the contact angle at about  $115^\circ$  [16]. Although the ratio of the PTFE to the activated carbon tends to be low (10-25%), it has a significant effect on the hydrophobicity of the sample which subsequently affects the effective capacitance for an aqueous electrolyte [16]. In comparison, the activated carbon cloths easily wicked in the salt solution. Although the surface areas are comparable as well as the underlying microstructure, we speculate that the underperformance of the activated carbon is likely attributed to the hydrophobic binder.

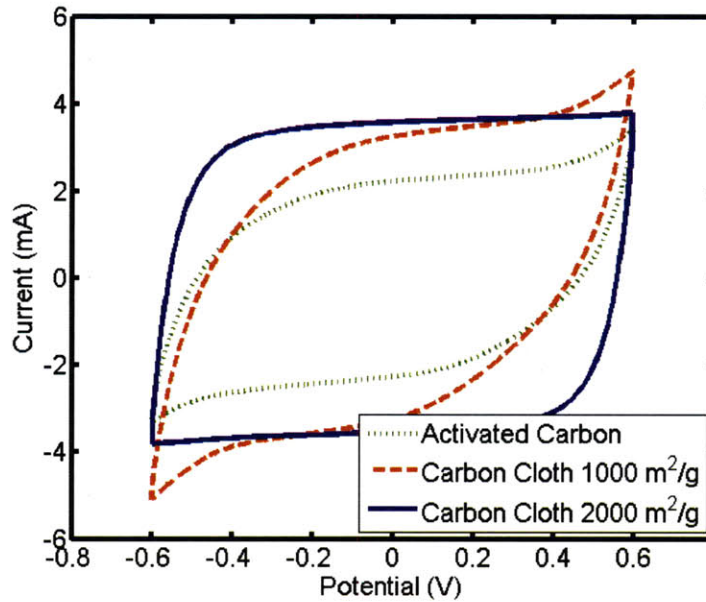


Figure 4-3: Cyclic voltammograms of the carbon cloths and activated carbon materials. In each test, an electrolyte of 1 M NaCl was used with a sweep rate of 10 mV/s. The capacitance for the material is given by the current divided by the scan rate.

It should also be noted that in general these electrochemical measurements suffer from a lack of repeatability. Even though the electrochemical cell construction can try to be replicated as closely as possible by using the same size electrode, volume of electrolyte, and spacer size, the CV diagrams often varied. Even in the CDI literature, there tends to be a lack

Material	Surface Area (m <sup>2</sup> /g)	Capacitance (F/g)
Carbon Cloth-20	2000	40
Carbon Cloth-10	1000	32
Activated Carbon	1200	25

Table 4.1: Capacitance values and approximate specific surface areas for the various electrode materials.

of continuity when comparing the CV diagrams across studies utilizing the same material. This overall repeatability is a major concern for obtaining an accurate representation of the material capacitance and requires further investigation.

Additionally, chronocoulometry was carried out on the various materials to further understand their behavior during the charging process. The electrodes were charged to various voltages and the current response was monitored. The current can be integrated to obtain the surface charge on the electrode over time. A sample response for the charge over time can be seen in Figure 4-4(a) for the 1000 m<sup>2</sup>/g carbon cloth charged to 0.3 V. Traditionally for dielectric capacitors in an RC circuit, the charge builds up on the surface exponentially in time with a time constant dependent on the value of the resistance  $R$  and capacitor  $C$  and equal to  $1/RC$ . Instead for electric double layer capacitors, this is not necessarily the case as diffusion limitations and additional resistances alter the charging dynamics. Faradaic supercapacitors that are diffusion limited are known to follow the Cottrell equation [31]:

$$i(t) = \frac{nFAD^{1/2}c_O}{\pi^{1/2}t^{1/2}}, \quad (4.3)$$

where  $F$  is Faraday's constant,  $n$  is the number of electrons needed to reduce the analyte  $O$ ,  $D$  is the diffusion coefficient,  $c_O$  is the bulk concentration of the reducible analyte,  $A$  is the electrode surface area, and  $t$  is time. Although this is not the specific form of the model for the electric double layer capacitor charging, we see that the capacitor in Figure 4-4(a) is not quite exponential like the dielectric capacitor and it's behavior can be explained from



diffusion effects.

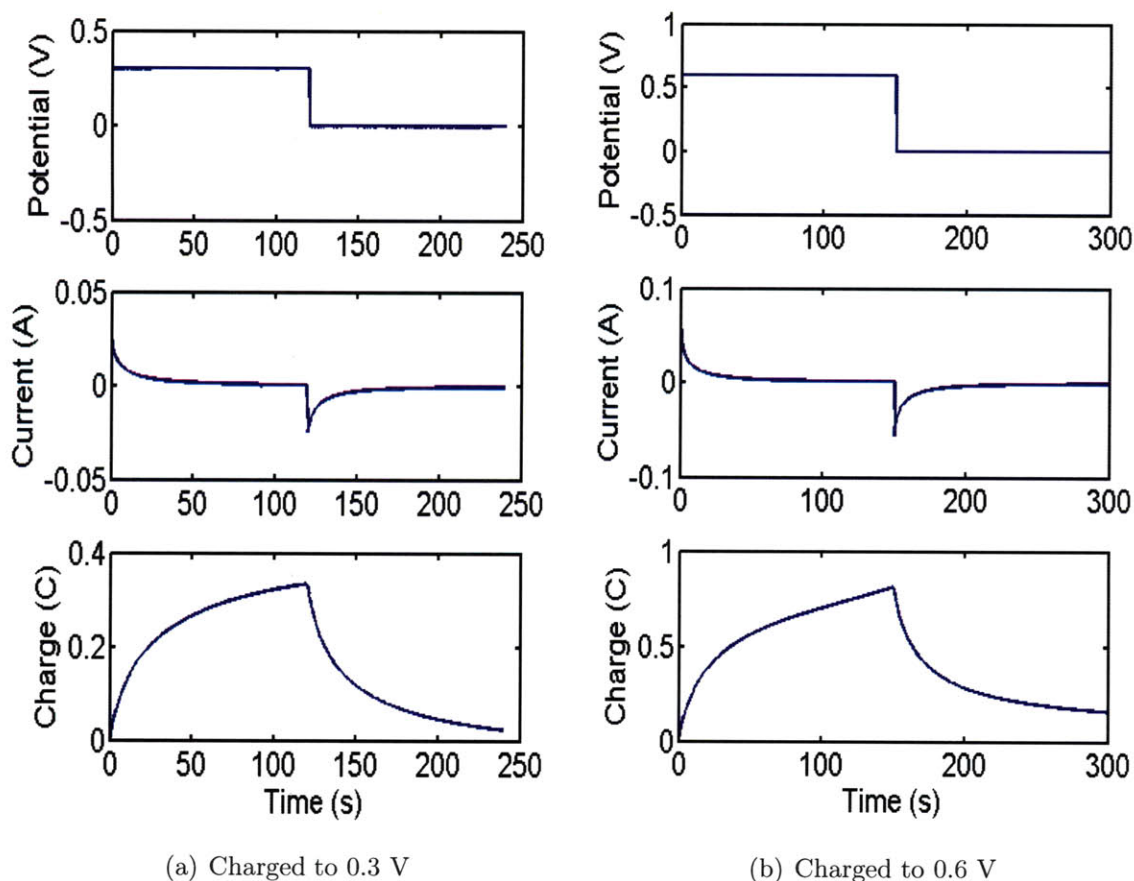


Figure 4-4: Chronocoulometry of the  $1000 \text{ m}^2/\text{g}$  carbon cloth charged to different voltages. The voltage, current, and charge versus time are all shown.

The same electrodes were then charged to a larger voltage of 0.6 V as in Figure 4-4(b). It should first be noted that from the current response, the corresponding  $1/e$  decay lengths for the 0.3 V and 0.6 V current responses are 7.89 s and 6.39 s, respectively. Instead of a constant RC time constant for the capacitor, this value instead varies depending on the voltage. Moreover, this time constant is significantly smaller than the minutes that it takes to fully charge the capacitor. Also, from the charge accumulation over time, it can be seen that the charge (especially in the 0.6 V charge case) does not appear to level off asymptotically

and continues to increase after a couple minutes of charging.

The lengthened charging times and the non-asymptotic behavior suggests that there are transport limitations due to the tortuous micropores in the activated carbon materials. As the capacitor continues to charge, over time ions are able to reorganize to enter harder to access pores. Additionally since the charging behavior of an electric double layer capacitor is in part due to the expulsion of co-ions from the double layer. At long time scales, all the co-ions should be expelled from the double layer, such that charging at longer times is simply due to extra counter-ions entering the double layer. These counter-ions may experience some diffusion limitations due to depletion of the counter-ions near the surface which additionally can lengthen charging times. Noting the charging times on the order of minutes and the potential diffusion limitations can have important implications for design of materials for capacitive deionization since ideal materials for the process would have decreased charging times to facilitate system throughput.

### **4.3 Silicon Microstructures**

One limitation of performing CV tests on the activated carbon-based materials is that it is difficult to gain physical intuition from comparing the capacitance values. Although each material has a reported surface area value from BET testing, this value is often times an overestimate of the actual surface area that can be accessed by the ions. Due to this limitation, we decided to investigate silicon microstructures where we can control the geometry during the fabrication. Because the standard length scales for electrokinetics tend to be small (on the order of 1 nm), in order to probe the ion transport mechanisms, the electrode features also must be on the order of nanometers. Although standard photolithography processes can create controlled structures, the size scale is limited by the diffraction limit of light to a couple hundred nanometers. In order to work around the diffraction limit, we used

a physical mask of polystyrene beads on silicon to define the feature size and create silicon nanopillars.

### 4.3.1 Nanopillars Fabrication

The nanopillars are fabricated using NIST standardized 50 nm polystyrene beads (Thermo Fischer Sciences) as a physical mask on highly doped silicon. The beads were suspended 1% by weight in an aqueous solution and mixed in a 1:1 solution with ethanol. The solution was spin-coated onto silicon wafers with a 330 nm thermal oxide layer. The wafers were subsequently etched using reactive ion etching. A gaseous mixture of  $\text{SF}_6$  and  $\text{O}_2$  etched through the oxide to create the nanopillars in the conductive silicon substrate. A cross-section of the nanopillars is seen in Figure 4-5(a). The resulting nanopillars are on average 50 nm in diameter and 200 nm in height, distributed throughout the entire substrate. Although the spacing is not controlled like the templated micropillars, the increase in surface area can be approximated to be about 13 times the planar area at maximum.

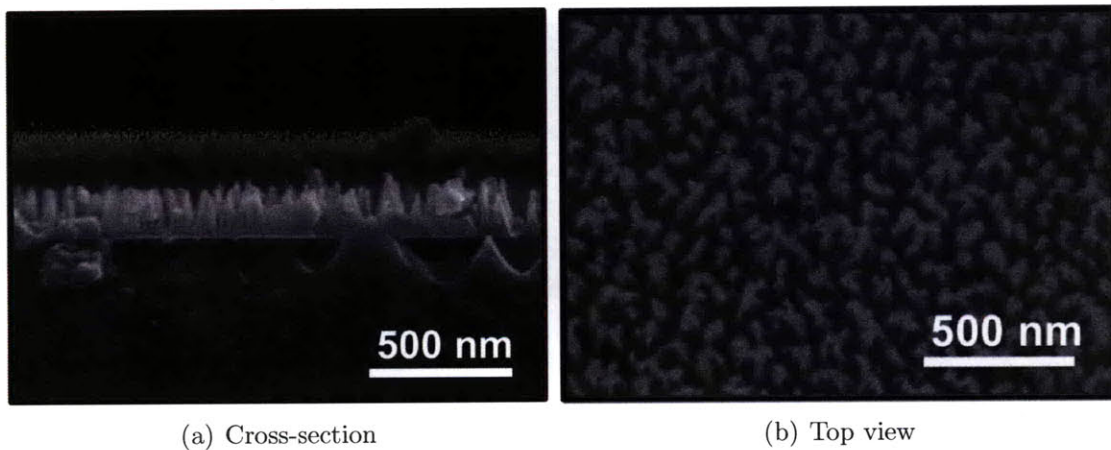


Figure 4-5: SEM images of the silicon nanopillars fabricated from polystyrene beads. The pillars measure about 50 nm in diameter and 200 nm in height.

### 4.3.2 Nanopillars Electrochemical Characterization

Electrochemical testing was also performed on the silicon-based electrodes shown in Figure 4-6. The average capacitance values were determined using a 1 M NaCl solution and a sweep rate of 50 mV/s. In each case, the electrodes were cycled 30 times, with the average capacitance values consistent across a 10 mV/s and 50 mV/s scan rate. The specific capacitance for the unpatterned silicon was 1.6 mF/g, the micropillars was 5.2 mF/g, and the nanopillars was 26 mF/g. The micropillars had a threefold increase in surface area to the unpatterned silicon, which is approximately matched by an equivalent increase in capacitance. The nanopillars, however, exhibited an increase in capacitance larger than the increase in surface area. Whereas the surface area increased by a factor of 13, the capacitance value is over 16 times that of the unpatterned silicon.

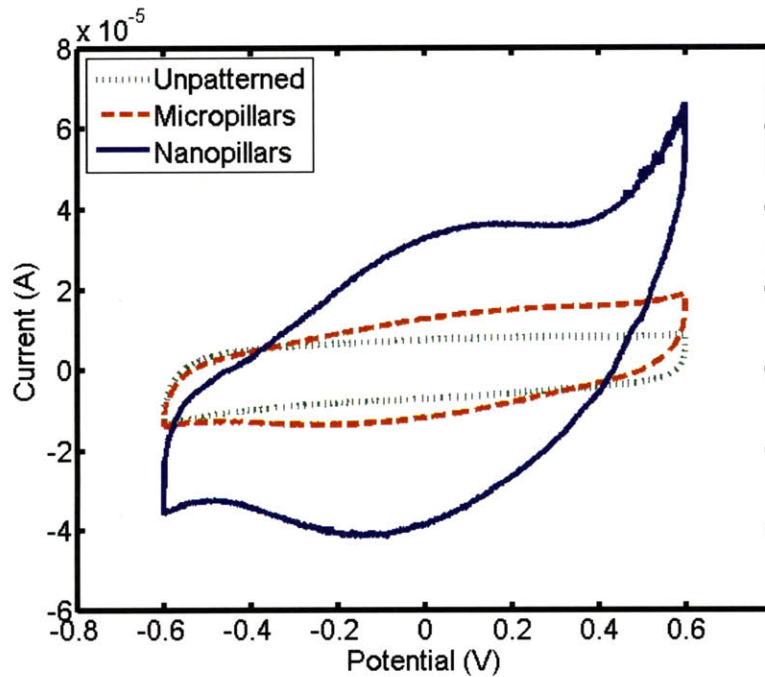


Figure 4-6: Cyclic voltammograms of the silicon-based materials. In each test, an electrolyte of 1 M NaCl was used with a sweep rate of 50 mV/s. The capacitance for the material is given by the current divided by the scan rate.

We speculate that this anomalous increase in capacitance may be attributed to a variety

of factors. First, the estimates in surface are difficult due to the non-uniform surface distribution of the nanopillars. In addition, there may be additional sulfur left on the electrode surface after fabrication due to exposure to  $\text{SF}_6$  plasma. Sulfur left on the surface may react in water at standard potentials of 0.447 V. The peak on the cyclic voltammogram at around 0.5-0.6 V may be an indication of this Faradaic reaction, thereby increasing the capacitance through pseudocapacitance. Lastly, there may also be geometrical advantages at this length scale, which can aid in the ion transport through restructuring of the electric double layer. However, further work must be performed to elucidate this large change in capacitance.

Electrochemistry measurements can only provide so much information for use in capacitive deionization. Ultimately the capacitance measurements must be correlated to electrosorption experiments to fully understand how a material will perform in CDI. A larger measured capacitance value obtained during cyclic voltammetry may not necessarily imply that it will exhibit more ion capture when compared to a material with a smaller capacitance [20]. Regardless, the electrochemical tests can allow insight into system charging dynamics providing a good starting point when choosing materials for CDI.

# Chapter 5

## Initial Flow Cell Experiments

To begin understanding the mechanisms governing salt capture in capacitive-based desalination, we created a miniature flow cell device to monitor the electrosorption behavior of various electrode materials. For the first iteration of the flow cell documented in this chapter, we focused on commercially available carbon-based materials. By correlating electrochemical measurements of the capacitance with measurements of electrode electrosorption, we hope to elucidate the relationship between the microstructure of the electrode and its potential effectiveness for capacitive deionization.

### 5.1 Design

The challenge in designing a test flow cell for testing the ion capture of electrode materials is that it both has to seal the fluid as well as make external electrical contacts to the electrode materials. The flow channel interfaced electrodes measuring 3 cm by 3 cm with a gap size of 3 mm separating the electrodes and an overall channel length of 10 cm. Figure 5-1 shows a schematic of the design. For the initial design, the channel was defined by two symmetrical acrylic pieces each with a 1.5 mm pocket sealed together by a gasket. Fluidic inlet and

outlet ports were added on the top surface which could be interfaced with a syringe pump to control the flow rate. Additionally, holes were created behind the electrodes to allow for an electrical connection. The electrode materials were interfaced with the acrylic channel by use of carbon tape.

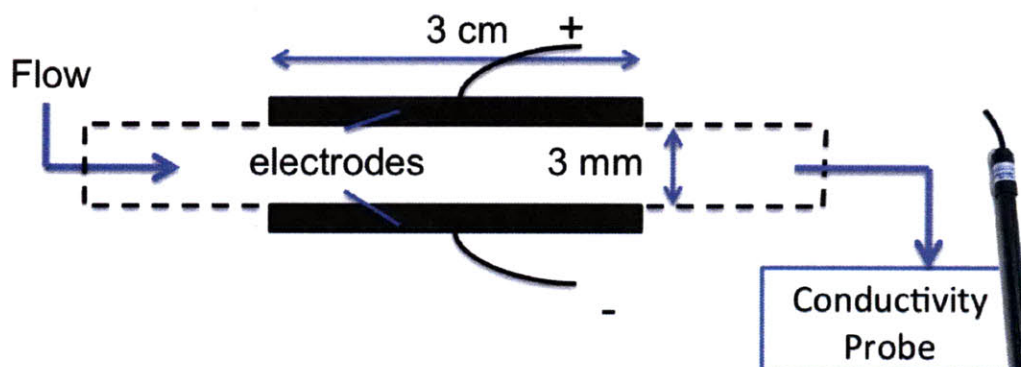
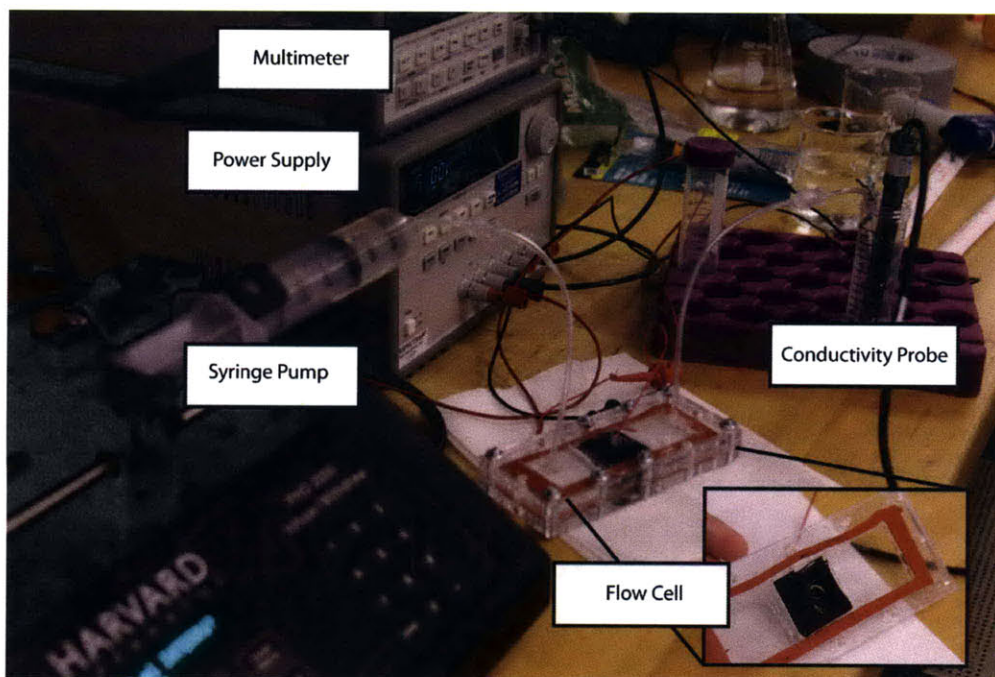


Figure 5-1: A schematic of the flow cell design. Electrodes measuring 3 cm by 3 mm are separated by a 3 mm gap size and are charged as salt water flows through the channel. A conductivity probe detects any changes in conductivity at the outlet.

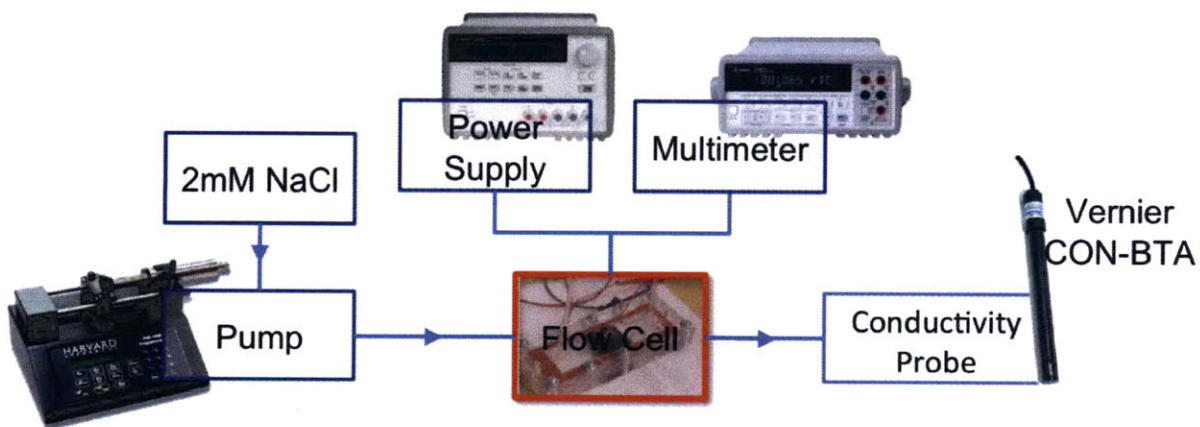
## 5.2 Experimental Setup and Instrumentation

The potential applied across the electrodes in the flow cell were controlled using a power supply (E3632A, Agilent) that supplied a step voltage. A multimeter (34401A, Agilent) then monitored the current response across the cell. The flow rate was controlled with a syringe pump (PHD 2000, Harvard), and the solution concentration monitored using a conductivity probe (CON-BTA, Vernier). The entire experimental setup is illustrated in Figures 5-2(b).

For testing, a 2 mM solution of NaCl acted as the stock feed solution. The solution first flowed through the device to fill up the cell and saturate the electrodes in the electrolyte. The flow stopped and the electrodes were subsequently charged to various voltages ranging from 1.2 V to 4 V. After the current decayed to 20% of its original value (about 15 minutes), the fluid was purged from the cell and the concentration accumulation at the outlet



(a) Photo of the experimental setup.



(b) Block diagram of the flow cell setup.

Figure 5-2: An electrolyte of 2mM NaCl is pumped through the flow cell as the electrodes are charged to various voltages while the current response and solution conductivity are monitored.



was monitored. This method is distinct from the actual capacitive deionization process in which the electrolyte is continually flowing. By continually flowing the standard electrolyte through the cell, this eliminates the potential effects of a diffusion transport limitation near the electrode surface. For the purposes of this initial cell, we decided to keep the fluid stagnant during the charging process primarily for ease of testing, however by monitoring the stationary fluid over time, it can also probe some of the additional diffusion effects involved in the transport of ions into the electrode pores.

### 5.3 Results and Discussion

By fully charging the electrodes with the electrolyte stationary, then flushing the cell into deionized water, the concentration profiles over time were obtained and shown in Figure 5-3 for the test case using 2000 m<sup>2</sup>/g activated carbon cloth electrodes. As expected, the larger the applied voltage, the larger the quantity of salt extracted from the solution [24]. The increase in electrosorption of the salt can be attributed to the larger surface potential which induces a longer electric double layer. Although the electrolysis of water occurs at a standard potential of 1.23 V versus the standard hydrogen electrode, in our experiment no electrolysis was observed even at the large applied voltages. In addition to the presence of an electrode resistance such that the surface voltage at the electrode-electrolyte interface is less than the applied voltage, it can also be attributed partly to the presence of charge carrying ions so that the applied surface energy is carried in the form of an ionic current instead of energy used to electrolyze the water. We still cannot eliminate the possibility of bubble growth within the electrode from electrolysis which is obscured from view. An additional effect of potential bubble growth within the electrode also may include reducing the active surface area, diminishing the total area involved in charging and ion capture.

By applying mass conservation to the concentration accumulation over time  $c$  in the

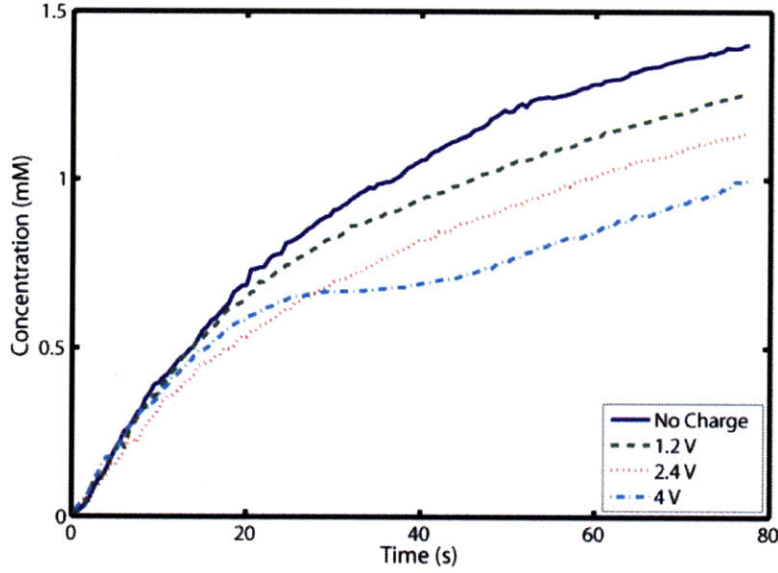


Figure 5-3: The concentration profiles over time for the accumulation of salt at the outlet for the flow cell charged to various voltages. The total salt absorbed by the electrodes is obtained by measuring the final concentration compared to the case when no voltage is applied.

control volume  $V$ , flow rate  $Q$  :

$$\frac{d}{dt}(cV) - Qc_{in} = 0 \quad (5.1)$$

we can extract the real-time concentration  $c_{in}$  at the outlet using numerical analysis of the total concentration data (the matlab code is found in Appendix C). This real-time concentration analysis is presented in Figure 5-4. Unfortunately the noise in the original concentration data is amplified in the numerical scheme when obtaining the real-time concentration data, so only general trends can be established. Because we have a laminar flow condition in the channel, the time axis can essentially be correlated to a position axis inside the flow cell since the electrodes were fully charged prior to purging the cell. As expected the solution concentration experiences a minimum which correlates to the center of the channel. However having charging times of approximately 15 minutes permits a concentration gradient to be established axially in the channel due to diffusion along the channel from the larger

concentration of ions in the bulk to the lower concentration of ions near the electrode. This diffusion effect is best exhibited by the 4 V charging scenario in Figure 5-4.

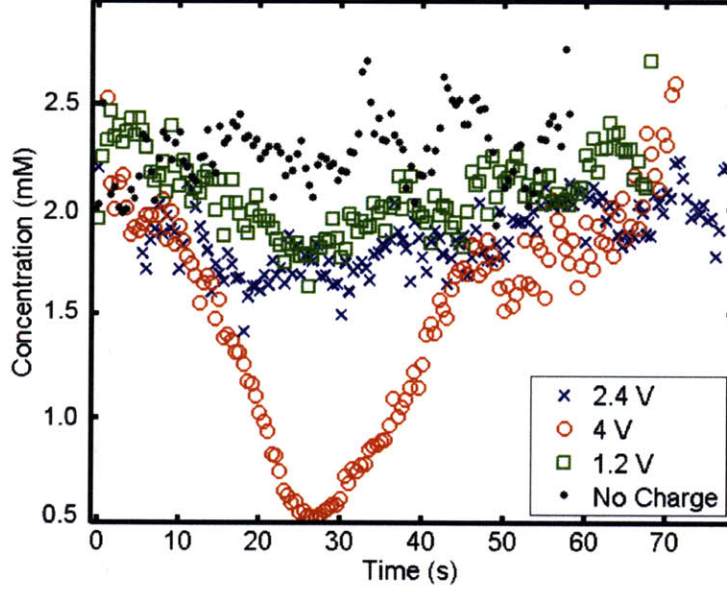


Figure 5-4: Real-time concentration data at the channel outlet over time as numerically determine from the concentration accumulation curves.

It is interesting to note that the general time required to fully charge the electrodes tended to be approximately 15 minutes, which is much larger than the tens of seconds it generally takes to charge and discharge supercapacitors [32]. This increased time required to charge the electrodes may be explained by diffusion limitations. We can estimate the timescale  $\tau$  for diffusion by:

$$\tau = \frac{L^2}{D} \quad (5.2)$$

where  $L$  is a characteristic length and  $D$  is the diffusion coefficient which can be estimated from the Stokes-Einstein relation:

$$D = \frac{k_B T}{6\pi\eta r} \quad (5.3)$$

where  $\eta$  is the fluid viscosity,  $r$  is the ion radius,  $k_B$  is the Boltzmann constant ( $1.38 \times 10^{-23}$  J/K), and  $T$  is the absolute temperature. Using the Eqn. 5.3, the diffusion coefficient is estimate to

be on the order of  $6 \times 10^{-10} \text{ m}^2/\text{s}$ , using the viscosity of water of  $10^{-3} \text{ Pa}\cdot\text{s}$  and the hydrated radius of 0.35 nm. For the observed experimental timescales of 15 min, from Eqn. 5.2 the diffusion length is estimated to be 0.7 mm. Since this diffusion length scale is a significant portion of half the channel height of 1.5 mm, we conclude that the charging timescales can be explained by a diffusion limitation for the transport of ions from the bulk solution to electrode. It should be noted that the above analysis provides a rough estimate for diffusion of ions into the bulk because the diffusion coefficient of the ion is known to decrease both in confined pore spaces as well as in the highly concentrated regions such as the electric double layer near the electrode surface [33].

Physically we can explain this diffusion limitation as a combination of processes as illustrated in Figure 5-5. As the ions begin to migrate to the electrode surface upon application of the voltage, a small area of fluid near the surface begins to deplete in charge while the bulk concentration remains unchanged. The lower concentration of ions near the surface consequently reduces the ease of transport to the surface in order to shield the large applied voltage. As time elapses, a concentration gradient builds up between the bulk fluid and this depletion layer near the surface. Slowly, ions from the bulk solution diffuse into these depletion layers and further to the surface to continue shield the charge. This reduces the bulk concentration, which is critical to the success of capacitive deionization, but also increase the time to charge the electrodes since it is essentially diffusion limited, with diffusion having a much longer timescale than the time required to form the double layer and shield the surface charge [24].

From the final concentration at the outlet, we extracted the total amount of salt removed from the system by the electrodes. For each of the electrodes the magnitude of this salt extraction with respect to the applied voltage is found in Figure 5-6. Two main trends should be noted. Firstly, the material with the highest capacitance had the most ion removal for any given voltage, while the material with the lowest capacitance had the least amount

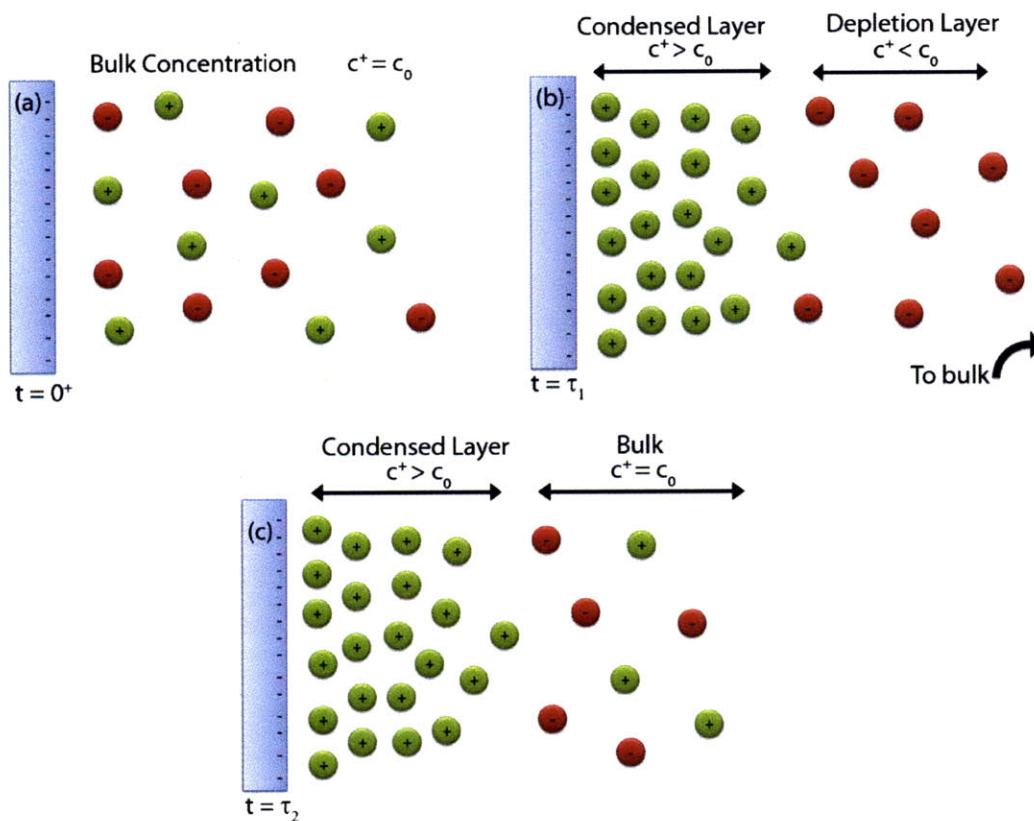


Figure 5-5: Schematic illustrating how diffusion occurs in the double layer. (a) The electrodes are not charged and the bulk concentration exists. (b) Once the electrodes are charged coions leave the double layer and counter ions enter the double layer which sets up a temporary depletion layer where the concentration of counterions is lower than in the bulk. (c) Over time counterions from the bulk diffuse into the depletion and a steady station concentration gradient is established.

of ion capture as expected from previous literature and theoretical models for ion capture [24]. However, it should be noted that in general, these measured electrosorption values were lower than most reported values in literature by about half [12, 15, 26]. This is most likely due to a combination of large contact resistances in the setup, but may also be somewhat attributed to diffusion limiting the transport and therefore electrosorption.

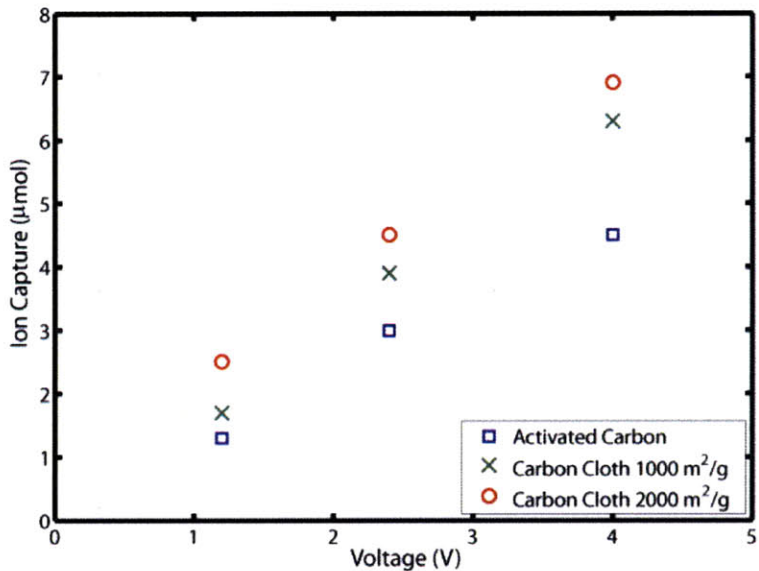


Figure 5-6: Shows the magnitude of ion capture with respect to voltage for the various carbon-based materials. The 2000m<sup>2</sup>/g exhibits the most ion capture for a given voltage while the activated carbon experiences the lowest.

The second trend to note is that for each type of electrode material, the ion capture is linear with respect to voltage [5, 30]. Due to shielding effects of the surface charge, it is expected that the concentration removed from the solution should be proportional to the surface charge. Moreover, from basic capacitor theory, the charge  $Q$  is equal to the capacitance  $C$  multiplied by the voltage  $V$ . It follows then that if the amount of ions removed is proportional to the surface charge, then the magnitude of ion removal should be proportional to  $C \times V$ . For a constant capacitance, this implies a linear trend between the applied voltage and the ion capture. For each material, if we multiply the applied voltage

by each of the respective capacitance values, we note that the three trend lines in Figure 5-6 reduce all to the same line in Figure 5-7. Since each of the materials are derivatives of activated carbon, they have a similar network of sub-micron tortuous pores although with a different morphology on the micron level. This result suggests that the transport limitations are associated with the sub-micron geometries.

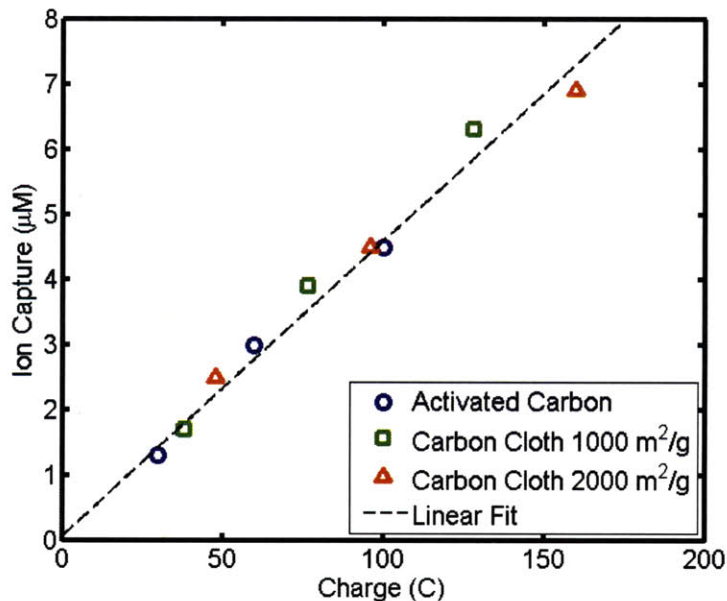


Figure 5-7: By using the material capacitance value, the applied voltage can be interpreted as an applied surface charge. After each data set is scaled by their respective capacitance, the data all collapse onto the same line.

What is of further interest to note is the magnitude of ion capture with respect to the magnitude of the surface charge. Using Faradays constant to convert the surface charge to moles of electrons, we note that this number is on the order of  $10^{-3}$  mol. However the measured ion capture was three orders of magnitude less and on the order of  $10^{-6}$  mol. This is in part due to the well-documented concept of charge efficiency where counter-ion adsorption and co-ion repulsion necessitate that the maximum ion capture by the electrode will be a fraction of the actual applied surface charge. Conceptually, since electrode charging is a dynamic process, as counter-ions move into the electric double to shield the surface charge,

at the same time co-ions that were previously near the surface move out of the double layer. This phenomenon causes the amount of actual salt capture on the electrode surface to be a portion of surface charge. Traditionally the value for the charge efficiency, defined as the magnitude of salt capture to surface charge, is always less than or equal to unity and in the range of 0.7-1 [24, 26, 30].

One possible explanation for the additional discrepancy between the surface charge and ion capture is the difference between ions in the diffuse part of the double layer versus the stagnant region, as well as ions within the pores versus ions outside the electrode surface. Even if the electrode was simply a flat plate, and a flow was applied, ions within the diffuse part of the double layer would flow with the fluid although they would still be acting to actively shield the surface charge. The ions within the Stern layer are stagnant and the fluid slip plane is defined at the outer Helmholtz plane. Although this is based off of theory for low applied voltages and dilute solutions, the same idea can be applied for large applied voltages. Although the distances from the electrode to the outer Helmholtz plane and the diffuse double layer are not well-defined, we can imagine that there is division between ions that are stationary and shielding the surface charge and mobile ions that shield the surface charge as they move with the streamlines. Unfortunately, theory coupling the hydrodynamics with the ion capture has yet to be developed.



## Chapter 6

# Microfabricated Flow Cell Redesign

With the first flow cell, we experienced major limitations performing the measurements. Because we used a commercially available conductivity probe, similar to the probes used in the literature, it was too large to physically insert into the channel to obtain real-time conductivity sensing data under flow conditions. Additionally, numerous problems were encountered while trying to make electrical contacts to the electrodes while simultaneously sealing out the fluid. Standard electrical wire could not be used if it was in contact with the fluid in the channel since it would allow for redox reactions, so we utilized platinum wire woven into the electrode. Initially, double-sided, electrically-conductive carbon tape was used to keep the electrodes in place, however trying to make an electrical connection directly to the carbon tape resulted in an addition resistance on the order of 1 k $\Omega$ . Because of the various challenges with the first flow cell, we decided to scale-down the system while integrating conductivity sensors at the inlet and outlet of the device to obtain real-time conductivity measurements of the fluid in a flow environment. Because during the real-time concentration measurements the concentration in the bulk is constantly replenished, we can further investigate the role of diffusion limitations during electrode charging.

## 6.1 Concept and Design

We chose to fabricate the new flow cell from silicon, using microfabrication techniques. This allowed us to integrate any potential electrode materials directly to the substrate as well as deposit additional electrodes to do the conductivity sensing. Also, by decreasing the channel gap size to less than 1 mm, we could increase the strength of the electric field, allowing for more efficient capture.

A schematic of the new design is in Figure 6-1. The flow channel consists of two symmetric pieces of silicon with the channel defined by a gasket between them. Depending on the material used, the gasket sizes ranged from 0.2 mm to 1.5 mm to account for the thickness of the electrodes. The silicon then extends out from the enclosed channel such that external electrical connections can be made. The silicon devices are sealed in an external clamp where the fluidic inlet and outlet ports are located. Initially, we attempted to instead laser ablate inlet and outlet ports directly onto the silicon, however upon initial use the holes served as a stress concentration and sheared the silicon upon the application of excess pressure.

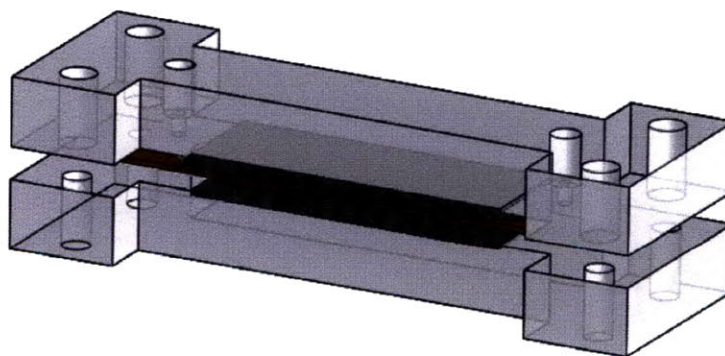


Figure 6-1: Model of the flow cell setup. The channel consists of two symmetric silicon devices with platinum electrodes separated by a gap controlled by the gasket thickness enclosed in a polycarbonate clamp.

The devices consist of three distinct regions as seen in Figure 6-2. In the center, a 2 by 2 cm area is reserved for placement of the primary adsorption electrodes. On either

side of the main electrodes, located 1 cm away, are additional platinum electrodes acting as conductivity sensors. As the salt water flows through the channel, the first set of platinum electrodes takes an initial reading of the conductivity. Then, after salt is adsorbed at the central set of electrodes, the latter set of platinum electrodes reads the conductivity to obtain a measure of the amount of salt removed from the system.

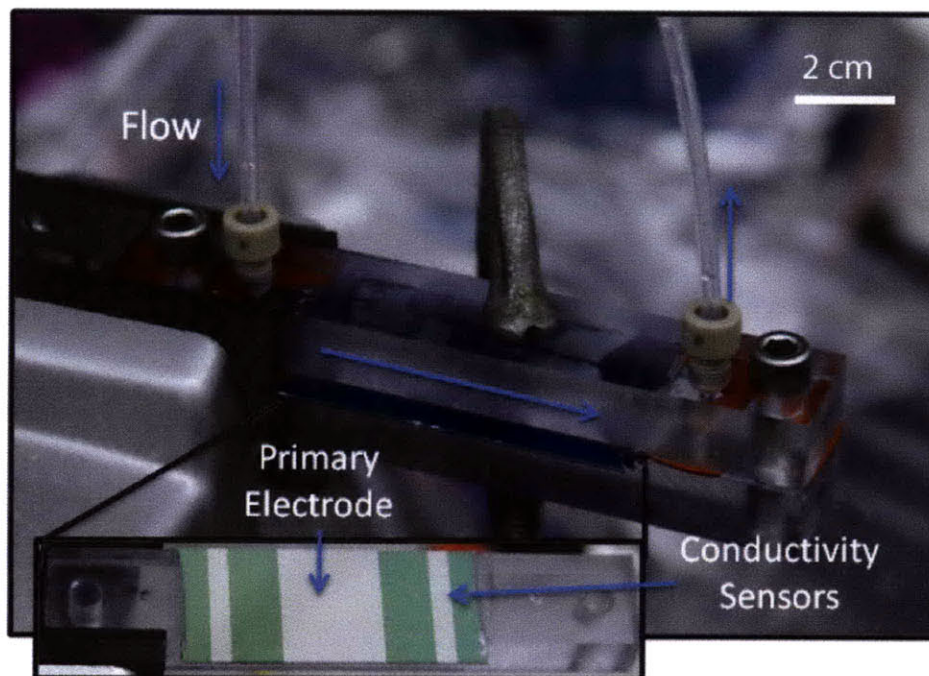


Figure 6-2: Photo of the redesigned flow channel. Each silicon device has three electrodes on it. The smaller two outer electrodes are used as conductivity sensors. The larger, inner electrode allows for various adsorption materials, such as carbon cloth, to be integrated into the flow setup.

### 6.1.1 Conductivity Sensors

Due to the small volume of fluid in the revised micro-flow cell, using a commercial conductivity probe was not an option. Instead, we decided to incorporate the conductivity sensors directly into the flow channel. Standard conductivity probes operate by having two or three inert electrodes and applying an AC voltage to measure solution resistance. If just

a DC voltage is used, shielding effects from the ions will skew the resistance readings. The use of an AC voltage disrupts the capacitive effects from double layer charging and instead isolates the solution resistance. Initially, we tested this concept using parallel stainless-steel plates immersed in various concentrations of sodium chloride solutions. We then applied a  $50 \text{ mV}_{\text{pp}}$  sine wave at various frequencies ranging from 1 kHz to 100 kHz and measured the cell resistance. As expected, the conductivity of the solution displayed a linear relationship to the concentration of the salt solution.

This proof of concept allowed us to apply the same concept to the microfabricated platinum electrodes. It was important to consider the geometry of the sensor with respect to the channel dimensions. A standard approximation for capacitors is that the electric field can be approximated by infinitely long flat plates separated by a small gap compared to the electrode area. Once the aspect ratio increases and the gap size becomes comparable to the length of the electrode, fringe fields must be considered. Initial testing for the platinum conductivity sensors focused on fabrication of electrodes of varying sizes ranging from 3 mm to 6 mm and with various spacings ranging from 3 mm to 6 mm in a test channel with a 1 mm gap size, illustrated in Figure 6-3. Using a potentiostat (1470E, Solartron Analytical) we input a  $50 \text{ mV}_{\text{pp}}$  1 kHz sawtooth wave and measured the current response. The use of a 1 kHz sawtooth wave was one limitation of using the potentiostat to measure the current response. The sampling rate was limited to 10,000 samples per second, so to fully capture the waveform and prevent aliasing a the 1 kHz frequency was chosen.

The current versus voltage for a variety of concentrations ranging from 5 mM to 10 mM is shown in Figure 6-4. The resistance of the solution is obtained from the slope during the charging and discharging steps according to Appendix C with a higher slope indicating a lower solution resistance and higher concentration. The hysteresis does represent that there was finite charging on the electrode surfaces during the cycling. This is to be expected given the timescale to form the electric double layer is on the order of 1 ns. Even with this

finite capacitance the frequency was fast enough such that the solution acted primarily as a resistor, which is confirmed by the fact that the slope of current verses voltage is the same during charging and discharging.

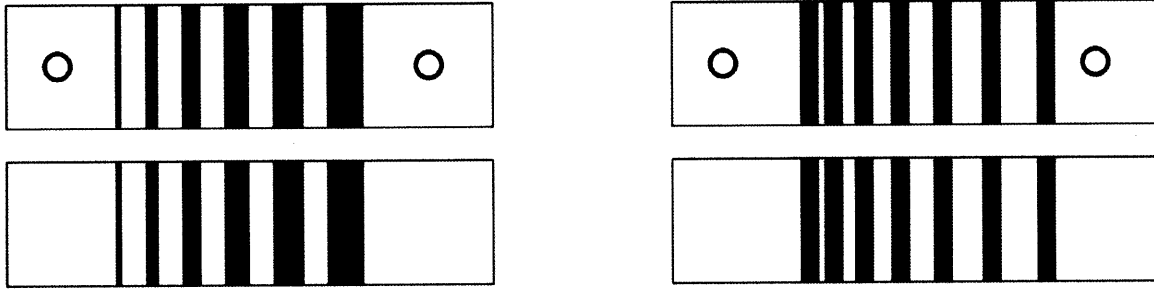


Figure 6-3: The spacing and the gap size between the platinum electrodes was varied on test silicon devices to determine if there was any affect on the measured conductivity. The left image shows a schematic of a device with the size of the platinum electrodes (black) varied, while the right image shows the spacing between adjacent electrodes varied.

## 6.2 Device Fabrication

Highly doped silicon was chosen as the primary support structure because of its flexibility in terms of fabrication options. Additionally, certain electrode materials, such as CNTs, may be directly grown onto a silicon substrate which can facilitate testing of those materials. The overall design of the silicon devices and process steps are shown in Figure 6-5. In order to electrically insulate the various sets of electrodes, we first grew a 330 nm thermal oxide layer on which all the subsequent materials could be deposited. The regions where platinum was to be deposited were next defined by photolithography. A 200 nm layer of platinum with a 20 nm titanium adhesive layer was then deposited by electron beam deposition. In addition to the conductivity sensors, additional platinum was patterned at the site of the primary electrodes such that other non-silicon based materials, such as activated carbon cloth, could be inserted into the channel using adhesive materials. A liftoff process removed the excess

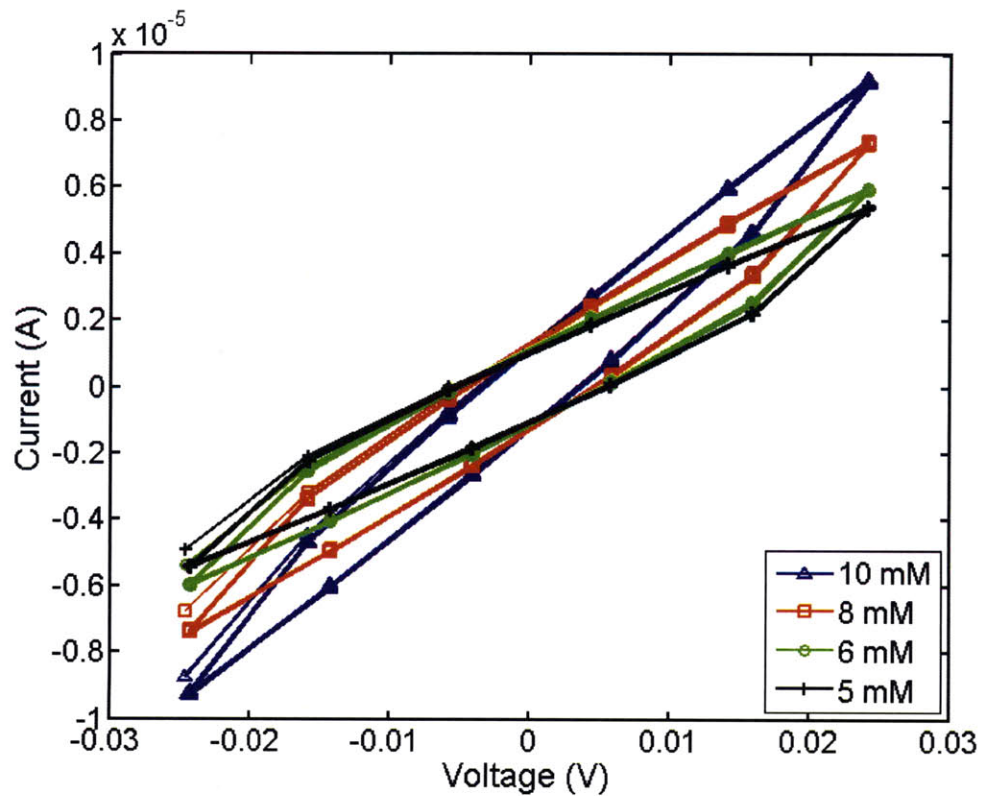


Figure 6-4: Electrolytes of different concentrations flowed through the channel and the conductivity was probed using a 1 kHz wave. The solution conductivity can be determined from the steady state slope and related linearly to the concentration.

platinum, and the devices were then ready to allow for the primary adsorption electrodes. A detailed account of the process used can be found in Appendix B.

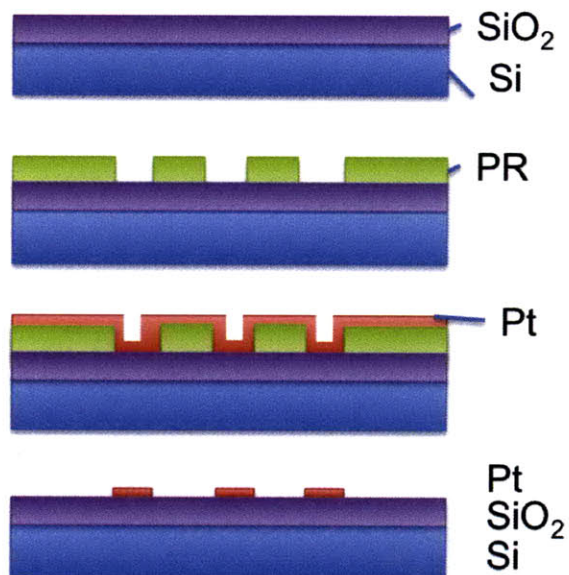


Figure 6-5: Fabrication process for the device. First a thermal oxide layer was grown on highly conductive silicon. The platinum electrodes were defined using photolithography and the platinum deposited through electron beam evaporation. Finally a liftoff process is used to remove any excess platinum.

### 6.3 Experimental Setup

To understand the electrosorption capability of the chosen electrode materials, a 1 mM NaCl solution was used as the feed solution as the electrodes were charged to a range of voltages. To allow for high resolution measurements, a potentiostat (1470E, Solartron Analytical) was used for all the electrical readings. A separate channel independently controlled each set of electrodes. The primary adsorption electrodes were given a step voltage input for 10 minutes, then held at 0 V for another 10 minutes to aid in the salt desorption. A syringe pump (PHD 2000, Harvard) controlled the flow through the channel. A baseline flow rate of 1 mL/min was used to allow for a seemingly constant bulk concentration between the

electrodes but still slow enough to provide sufficient resolution for conductivity sensing.

## 6.4 Results and Discussion

The transient concentration behavior of the system is displayed in Figure 6-6. At time 0 a step voltage of either 1.2 V was applied and the solution conductivity and cell current was probed every second. Shortly after the voltage is applied, the current decays rapidly, and we also observe a decrease in the effluent solution concentration indicating electrosorption of ions on the electrodes. It is interesting note how the current decays to a nonzero value which is on the same order compared to the peak current. A nonzero steady-state current may indicate that Faradaic side reactions are occurring which is a possibility if there is any contamination on the electrode material. Another explanation is that although the current appears to be at a steady-state value, it may be slowly decaying at a time scale much longer than the experiment. Given that some electrochemical capacitors can take hours to charge this response is also feasible. Additionally, the asymmetry in the reduction of concentration requires further examination. Upon application of the voltage the concentration reduces much quicker than the time required for the concentration to increase back to the initial value as the electrodes begin to saturate.

Although it is evident that the rise in the effluent concentration is due to the limited capacity of the electrodes for salt capture, it is not immediately clear what dictates the slower time for the concentration rise to occur compared to the concentration depletion. This asymmetrical profile was also obtained in the theoretical model predicted by Biesheuvel *et al.* [26]. Since their model simplifies the ion transport by assuming a stagnant mass-transfer layer near the electrode surface and ignores electrode porosity, the electrode salt adsorption depletes the mass-transport layer of its ion concentration and forces additional ions to diffuse from the bulk over time. This diffusion into the electrode occurs as the electrode becomes



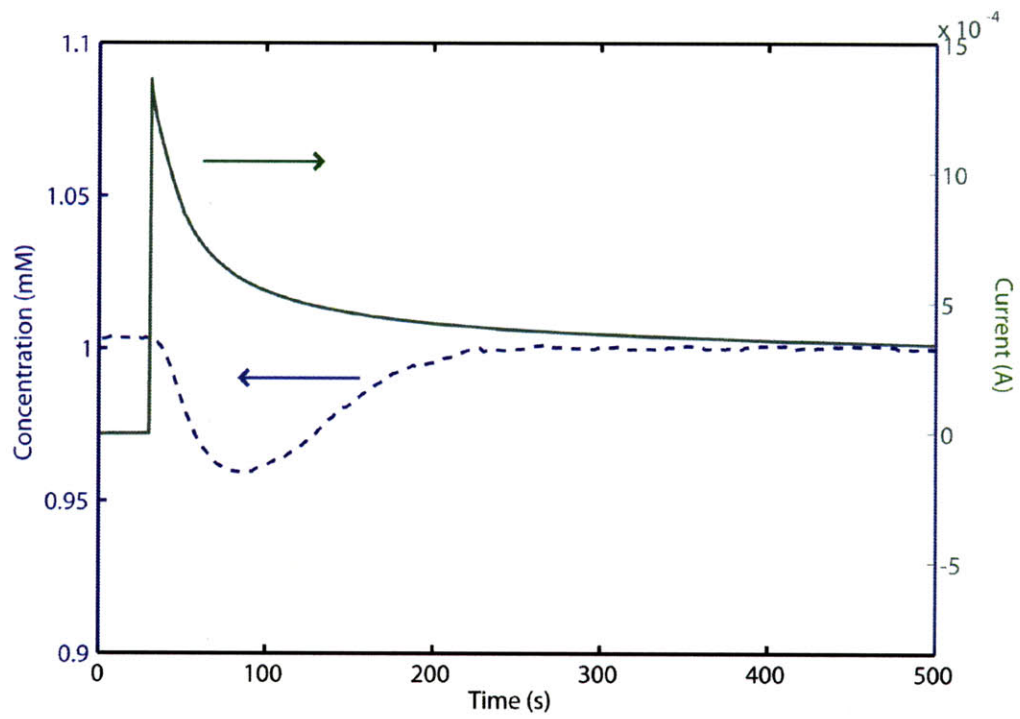


Figure 6-6: Transient concentration and current response for the carbon cloth charged to 1.2 V at a flow rate of 1 mL/min.

saturated and therefore slows the rise in the solution concentration.

In general, it should be noted that the charging times for this scaled-down flow cell are much smaller than the 15 minutes needed to charge the previous flow channel design. From Figure 6-6 it is clear that the electrode becomes saturated within about 3.5 minutes after the voltage is applied. The main motivation for this sharp decrease in charging times is due to the introduction of convective mass transport. Since the influent stream is at a constant concentration, diffusion only needs to occur in a small region locally near the electrode surface. However, the length of this timescale still indicates that diffusion is still a dominant factor in this system since the charging time exceeds the standard timescale of  $\tau_C = \lambda_D L/D$ , where  $\lambda_D$  is the Debye length,  $L$  is the separation between the electrodes, and  $D$  is the diffusivity, for diffuse charge dynamics in electrochemical cells [24].

In addition to the 1.2 V electrode charging which was probed by Biesheuvel *et al.* and the majority of the literature in order to avoid any potential electrolysis of water at higher voltages, we also decided to charge the electrodes to 2 V and 4 V. Like in the previous flow cell setup no electrolysis of water was actually observed however it does not eliminate the possibility of bubble growth within the electrode which is shielded from view. Since the resistance between the electrical contacts and the electrode surface was measured to be approximately 100  $\Omega$  and the current peak was in the milliamp range, the voltage drop across the electrodes should have been on the order of 0.2 V implying that the electrode-electrolyte interface was at a potential larger than 1.23 V.

Although it is visually unclear whether or not electrolysis occurs in the 2 V and 4 V charging cases, it is nonetheless interesting to note the transient concentration behavior of the effluent fluid in Figure 6-7. Unlike the asymmetrical adsorption curve in the 1.2 V case as corroborated by the Biesheuvel *et al.* model, both the 2 V and the 4 V charge the transient response of the concentration appears more symmetrical with the exception of an overshoot in the steady state effluent concentration. Fundamentally, it appears as if there is an additional

mechanism controlling the ion capture in the 2 V and 4 V case compared to that of the 1.2 V charge. In fact, this may be a clear indication of electrolysis. If electrolytic bubble growth occurs at distinct nucleation sites within the electrode surface, this can effectively decrease the active electrode area for ion capture. Upon application of a voltage the electric double layer forms almost instantaneously, in the absence of diffusion limitations, at a timescale of  $\tau_D = \lambda_D^2/D$  which is on the order of nanoseconds [24]. As electrolysis begins to occur, gas may form inside the pores displacing the electrolyte and inserting additional ions into the effluent stream until a steady state is reached and some maximum amount of pore area is obstructed. Further experiments must be performed probing this regime beyond the overpotential for water electrolysis to definitively determine the mechanism controlling this concentration overshoot.

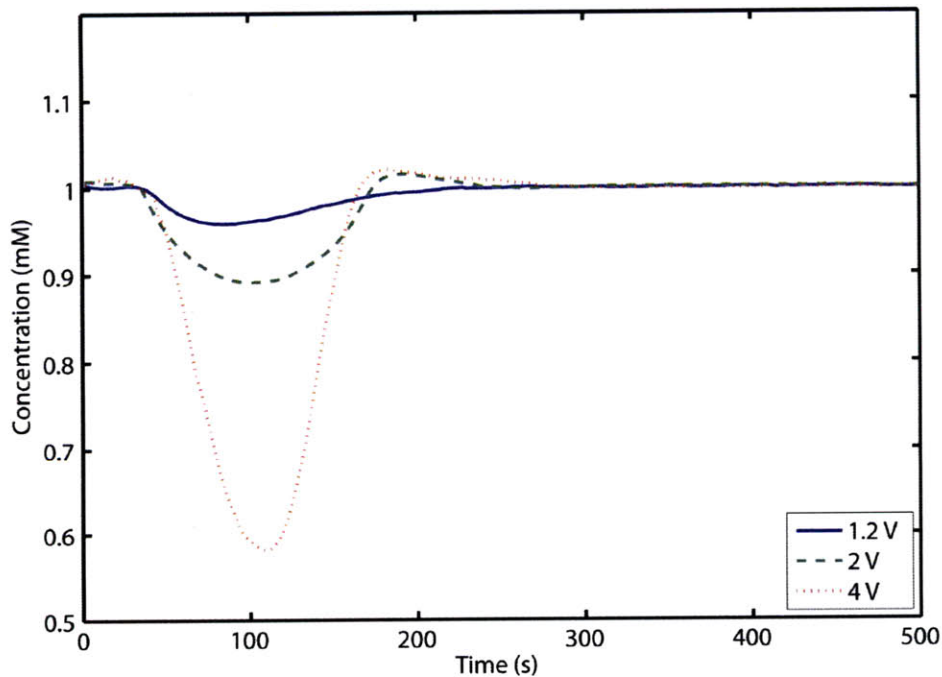


Figure 6-7: The transient concentration response for the carbon cloth for varying voltages.

The transient concentration response can also be integrated over time to obtain the total

amount of ion capture on the electrodes, Table 6.1. The electrosorption capacity for the 1.2 V charge is on par with reported values in the literature for activated carbon cloth [12, 15, 26] unlike in the previous flow cell. It is interesting to note that unlike the well defined linear relation in the diffusion-based flow cell and in the linear for small applied voltages [30], here the trend is not as obvious. The results seem to suggest that there may be some optimal voltage at which ion capture is a maximum that may be beyond the overpotential. Additionally, there may be additional effects through partial desolvation of the ions at the larger voltages to access smaller pores as suggested by recent work in supercapacitors [34–37].

However, because of the complex geometry of the electrode and the uncertainty of electrolysis, we cannot make any certain recommendations. Further work is needed in a simpler geometry such as a flat plate or well ordered pores and in an orientation where the electrode surface can be observed while charging to allow for such conclusions. Regardless, probing the range of cell voltages beyond 1.2 V is not currently seen in the CDI literature, but may provide further insight into designing the optimal electrode setup for desalination.

Applied Voltage (V)	Salt adsorption ( $\mu\text{mol/g}$ )	adsorption per Voltage ( $\mu\text{mol/gV}$ )
1.2	63.5	52.8
2	125.9	63.0
4	239.4	59.9

Table 6.1: Salt adsorption for the miniature flow channel displayed according to the applied voltage.

## 6.5 Measurement Challenges

The measurements described above were not without challenges. We experienced setbacks both in the device assembly as well as during data acquisition. Although the microfabricated flow channel addressed some of the main challenges of the larger flow cell design, there were

still many drawbacks. Gaskets aid in sealing the channel, however they provide a nonuniform gap height and variability once the flow cell is disassembled and reassembled since the gasket compression is a function of the applied clamping pressure. Future revisions should set a controlled channel height with a more rigid material that is about 1 mm in thickness and employ a thinner gasket of approximately 100  $\mu\text{m}$  to provide fluidic sealing.

One of the unexpected challenges with the microfabrication was the diffusion of the 20 nm titanium layer through the 330 nm thermal oxide causing electrical shorting between the electrodes. Future channel revisions can instead directly sputter the platinum onto the polycarbonate channel fixture which would ensure that there is no electrical shorting. Also, this would allow the adsorption electrode material to be slightly recessed in the channel. The activated carbon cloth is quite thick, 0.5 mm, compared to the desired channel thickness. Because of the thickness mismatch, we encountered electrical shorting across the channel between the two adsorption electrodes due to interactions from stray carbon fibers.

During the measurements, many of the challenges we faced were with the conductivity sensors. In numerous runs the resting potential of the platinum conductivity sensors varied from before and after the run, for example increasing from 30 mV to 120 mV. Although the cause of this is currently unknown, it may be due to surface conduction near the electrode surface from the large concentration of counterions near the surface affecting the adjacent electrodes. Moving the sensors farther away from the carbon electrodes can mitigate this effect. Moreover, the repeatability of the sensor conductivity measurements was often questionable. Many runs would produce faulty data, as for example in Figure 6-8, where during charging the solution concentration increases beyond the initial concentration, there are discontinuities in the conductivity readings, and upon discharge the solution concentration decreases.

Discharging was in general very difficult to measure, and we have yet to obtain a run with a clean discharge curve. It still remains unclear whether the lack of repeatability during

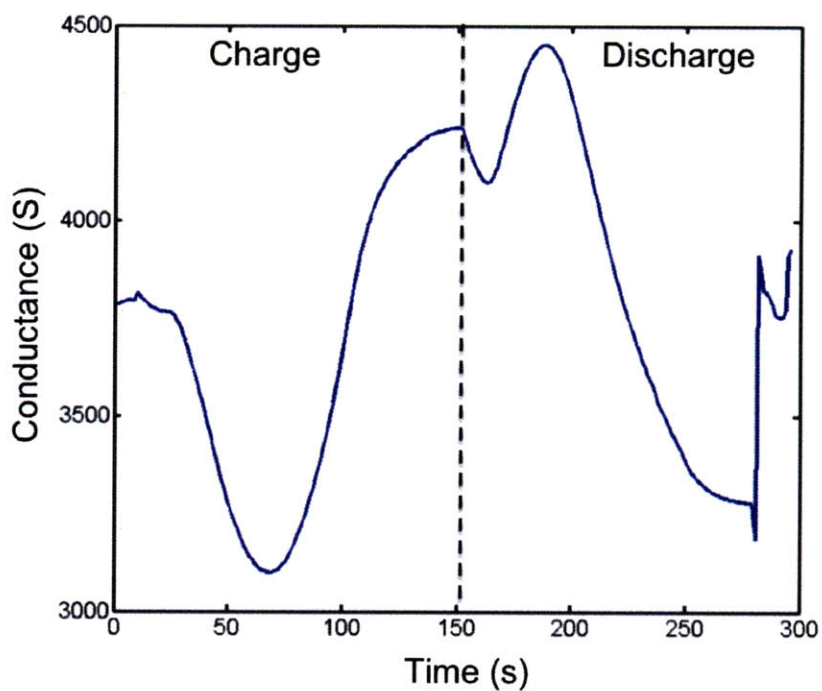


Figure 6-8: An example of faulty data obtained during testing.

discharge was purely an instrumentation issue or also stemmed from physical problems during discharge. Once the step voltage is released and the potentiostat regulates the potential at 0 V, the ions may take a much longer time to diffuse out of the electrode than to enter during charging with an applied electric field. Regardless, this cannot explain the non-physical discharge behavior in Figure 6-8 and may stem from the same underlying cause as the increase in the platinum electrode resting potential after a run. Relocation of the sensors farther away from the adsorption electrodes may also help this measurement issue, however, only a flow cell redesign will provide definite conclusions.

The experiments detailed in this chapter studying ion capture on carbon-based electrodes still require further trials in order to better understand the relationship between capacitance and ion capture. The first step would be another redesign of the flow channel setup according to these recommendations. This experimental redesign and other potential experiments will be further addressed in Chapter 7.

# Chapter 7

## Summary and Future Directions

In this study we initiated our understanding of ion transport in capacitors for water desalination applications. Although the literature tends to focus mainly on development of novel materials for capacitive deionization, there is still a general lack of understanding of the micro- and nanoscale transport that governs the charging process. By beginning to relate electrochemical measurements of capacitance to flow cell conductivity measurements, we can gain insight into the underlying physics. From the charging timescales in both the initial and redesigned flow cell, we can conclude that capacitive deionization is fundamentally a diffusion limited process. Opportunities exist to limit this diffusion limitation in order to greatly improve charging times.

Additionally, we can examine the difference in salt adsorption between the first and second flow cells in Table 7.1. Although the old flow cell exhibited large electrical losses from the electrode connections, the difference in capture between the two flow channels cannot completely be accounted for from electrical losses and may be attributed to the electrokinetics. Further investigation is required, as it is unclear if the charging in the first flow cell with stagnant fluid with extended charging times affected the steady state electrosorption in the electrode. Furthermore, because of the large gap size in the first cell,

the applied electric field was reduced. Although the electric field serves as a driving force for electromigration, it is unclear if this also affects the ion capture in the electrode. Overall, these experiments must be revisited to isolate the primary causes for the electrosorption discrepancies and explore the ion capture potential as a function of applied potential.

Applied Voltage (V)	Old Cell adsorption ( $\mu\text{mol/g}$ )	New Cell adsorption ( $\mu\text{mol/g}$ )
1.2	63.5	33.1
2	125.9	57.6
4	239.4	94.3

Table 7.1: Salt adsorption for the first and second flow channels for the 2000  $\text{m}^2/\text{g}$  carbon cloth displayed according to the applied voltage.

Moreover, further work to understand the system dynamics must be accomplished in order to better tailor materials specifically for desalination systems. Although theory has started to be developed to understand simplified, model electrode geometries, it has not yet evolved to be able to make design recommendations for CDI systems or even been experimentally validated. More controlled experiments need to be performed on these model geometries both to corroborate the theoretical aspects of capacitive charging and also to probe additional transport phenomena not yet addressed in the literature.

## 7.1 Future Directions

### 7.1.1 Carbon Electrode Study Redesign

Once a redesigned flow channel is in place, following the recommendations in the previous chapter, a systematic approach should be taken in future experiments to ensure repeatability. The material needs to be first be submerged in salt water for a prolonged amount of time to discard the effect of physical adsorption such that the experiment isolates salt capture due to electrosorption. Additionally, prior to each test the material should be cycled using



cyclic voltammetry to ensure that the electrodes return to a point of zero charge. Different voltages can then be probed starting from less than a volt to 4 V to further examine the range of voltages above and below the overpotential. It would also help in this setup to use a three-electrode setup instead of the two-electrode symmetric setup as is currently used. The addition of a reference electrode can ensure that each electrode is being charged to a voltage in reference to a known potential facilitating the identification of any potential chemical reactions.

In addition to the carbon cloth, this setup could incorporate a variety of standard electrode materials. Besides other surface area carbon cloths, carbon nanotube (CNT) electrodes are another potential electrode material. CNT forests of various lengths and packing densities can be grown. However, a similar limitation with the CNT electrodes still exists: a lack of structure in the morphology to help determine the actual surface area. Since current technology for surface area measurements, BET testing, is inaccurate and overestimates the actual surface area, a true relationship between surface area and ion capture difficult to obtain.

### 7.1.2 Controlled Geometries

Instead of nonuniform, tortuous pores as in the activated carbon-based electrodes, an ordered electrode structure with a controlled pore size distribution in the nanometer range must be investigated. It is for this model geometry that the most insight may be obtained for the capacitive charging and ion capture. By systematically decreasing the pore size from about 10 nm to sub-nanometer pore sizes, smaller than the solvated ion diameter, we can controllably introduce steric limitations. For the larger mesopores, larger than approximately 2 nm, we expect the ion capture to be fairly predictable, following both theory and the capacitance. At some point, once the size of the pores becomes comparable to the size of the double layer and the ionic diameter, it is unclear how the material will perform both for

electrosorption and capacitive charging.

One potential material that can facilitate these experiments is ordered mesoporous carbon [38]. These materials self-assemble into a mesoscale structures (2-50 nm) with an overall uniformity. Porous alumina provides another opportunity due to the high control over pore sizes; however, unlike ordered mesoporous carbons, alumina is not electrically conductive. Additional processing is needed in order to use porous alumina as an electrode material. One such idea is to use atomic layer deposition or electroless plating to deposit a gold or platinum layer on the alumina to make the electrode conductive. Either of these materials provides an opportunity for investigating ion transport because of the high level of control in the morphology during synthesis allowing features to be created on the same order of critical electrokinetic length scales.

Additionally for this porous electrode geometry there may be benefits for charging to voltages larger than the electrolysis potential because of ion solvation effects [34], if it is not offset by a reduced area effect from electrolytic gas formation. Ideally electrical measurements will be coupled with high-resolution imaging to enhance understanding of electrolysis within porous electrodes.

### **7.1.3 Electrokinetics near a Flat Plate**

Ideally the first experiments to be performed should be electroadsorption experiments on a flat plate, in order to experimentally validate newly developed theory for electrokinetics at high voltages [23, 25, 39]. Either platinum or indium titanium oxide (ITO) glass electrodes would be used to probe the flat plate geometry. However, first more sensitive conductivity sensors must be developed. Since the capture on a flat plate will be two to three orders of magnitude less than that on porous electrodes, the conductivity sensors must be able to resolve nanomolar changes in concentration. This will require a fundamentally different channel geometry with a well-defined spacing unlike the previous design with gasket material

that can vary in height depending on the applied pressure. Additionally, high-resolution circuitry is needed to sense the smaller signal changes. Once the proper instrumentation has been established, in addition to monitoring electrosorption on the electrode surfaces, we can also probe ion capture at higher aqueous voltage where electrolysis may occur. This range has not yet been addressed in the literature and may provide more insight by imposing additional transport limitations.

Capacitive deionization is a promising technology that can aid the widespread water crises. Although it has been proven to be a functioning technology, much is still unknown as to the governing physics. Future experiments should focus on understanding the ion transport within nanometers of the electrode-electrolyte interface. This should be accomplished by investigating standard commercial electrode materials, such as activated carbon derivatives, newly developed controlled mesoporous geometries, such as porous alumina and ordered mesoporous carbon, and simple planar electrodes. This understanding can greatly enhance the ability to tailor materials to enhance transport into the pores. On the macroscopic level, this manifests itself as enhanced efficiency in electrosorption materials, which can help make CDI a more marketable desalination technology.

# References

- [1] J. E. Miller, “Review of water resources and desalination technologies,” *SAND REPORT*, pp. 1–54, Mar 2003.
- [2] M. A. Shannon, P. W. Bohn, M. Elimelech, J. G. Georgiadis, B. J. Marinas, and A. M. Mayes, “Science and technology for water purification in the coming decades,” *Nature*, vol. 452, pp. 301–310, Jan 2008.
- [3] N. R. C. Committee on Advancing Desalination Technology, ed., *Desalination: A National Perspective*. Washington, D.C.: The National Academies Press, 2008.
- [4] C. Fritzmann, J. Loewenberg, T. Wintgens, and T. Melin, “State-of-the-art of reverse osmosis desalination,” *Desalination*, vol. 216, pp. 1–76, Jan 2007.
- [5] A. Johnson and J. Newman, “Desalting by means of porous carbon electrodes,” *J Electrochem Soc*, vol. 118, pp. 510–&, Jan 1971.
- [6] R. Pekala, J. Farmer, C. Alviso, T. Tran, S. Mayer, J. Miller, and B. Dunn, “Carbon aerogels for electrochemical applications,” *Journal of Non-Crystalline Solids*, vol. 225, pp. 74–80, Jan 1998.
- [7] J. Farmer, D. Fix, G. Mack, R. Pekala, and J. Poco, “Capacitive deionization of  $\text{nh}_4\text{cl}_4$  solutions with carbon aerogel electrodes,” *Journal of applied electrochemistry*, vol. 26, pp. 1007–1018, Jan 1996.

- [8] J. Farmer, D. Fix, G. Mack, R. Pekala, and J. Poco, "Capacitive deionization of nacl and nano3 solutions with carbon aerogel electrodes," *J Electrochem Soc*, vol. 143, pp. 159–169, Jan 1996.
- [9] P. Simon and Y. Gogotsi, "Materials for electrochemical capacitors," *Nature Materials*, vol. 7, pp. 845–854, Jan 2008.
- [10] E. Avraham, B. Yaniv, A. Soffer, and D. Aurbach, "Developing ion electroadsorption stereoselectivity, by pore size adjustment with chemical vapor deposition onto active carbon fiber electrodes. case of  $ca^{2+}/na^{+}$  separation in water capacitive desalination," *J Phys Chem C*, vol. 112, pp. 7385–7389, Jan 2008.
- [11] H.-J. Ahn, J.-H. Lee, Y. Jeong, J.-H. Lee, C.-S. Chi, and H.-J. Oh, "Nanostructured carbon cloth electrode for desalination from aqueous solutions," *Mat Sci Eng A-Struct*, vol. 449, pp. 841–845, Jan 2007.
- [12] H.-J. Oh, J.-H. Lee, H.-J. Ahn, Y. Jeong, Y.-J. Kim, and C.-S. Chi, "Nanoporous activated carbon cloth for capacitive deionization of aqueous solution," *Thin Solid Films*, vol. 515, pp. 220–225, Jan 2006.
- [13] X. Z. Wang, M. G. Li, Y. W. Chen, R. M. Cheng, S. M. Huang, L. K. Pan, and Z. Sun, "Electrosorption of ions from aqueous solutions with carbon nanotubes and nanofibers composite film electrodes," *Appl Phys Lett*, vol. 89, p. 053127, Jan 2006.
- [14] C. Yang, W. Choi, B. Na, B. Cho, and W. Cho, "Capacitive deionization of nacl solution with carbon aerogel-silica gel composite electrodes," *Desalination*, vol. 174, pp. 125–133, Jan 2005.
- [15] M. Ryoo, J. Kim, and G. Seo, "Role of titania incorporated on activated carbon cloth for capacitive deionization of nacl solution," *J Colloid Interf Sci*, vol. 264, pp. 414–419, Jan 2003.

- [16] J.-B. Lee, K.-K. Park, S.-W. Yoon, P.-Y. Park, K.-I. Park, and C.-W. Lee, "Desalination performance of a carbon-based composite electrode," *Desalination*, vol. 237, pp. 155–161, Jan 2009.
- [17] S. Brunauer, P. Emmett, and E. Teller, "Adsorption of gases in multimolecular layers," *J. Am. Chem. Soc.*, vol. 60, pp. 309–319, Jan 1938.
- [18] Y. Gao, L. Pan, H. Li, Y. Zhang, Z. Zhang, Y. Chen, and Z. Sun, "Electrosorption behavior of cations with carbon nanotubes and carbon nanofibres composite film electrodes," *Thin Solid Films*, vol. 517, pp. 1616–1619, Jan 2009.
- [19] X. Z. Wang, M. G. Li, Y. W. Chen, R. M. Cheng, S. M. Huang, L. K. Pan, and Z. Sun, "Electrosorption of nacl solutions with carbon nanotubes and nanofibers composite film electrodes," *Electrochem Solid St*, vol. 9, pp. E23–E26, Jan 2006.
- [20] L. Li, L. Zou, H. Song, and G. Morris, "Ordered mesoporous carbons synthesized by a modified sol-gel process for electrosorptive removal of sodium chloride," *Carbon*, vol. 47, pp. 775–781, Jan 2009.
- [21] E. Nightingale, "Phenomenological theory of ion solvation - effective radii of hydrated ions," *J Phys Chem-US*, vol. 63, pp. 1381–1387, Jan 1959.
- [22] H. Ohtaki and T. Radnai, "Structure and dynamics of hydrated ions," *Chem Rev*, vol. 93, pp. 1157–1204, Jan 1993.
- [23] P. M. Biesheuvel and M. Z. Bazant, "Nonlinear dynamics of capacitive charging and desalination by porous electrodes," *Phys. Rev. E*, vol. 81, p. 031502, Jan 2010.
- [24] M. Bazant, K. Thornton, and A. Ajdari, "Diffuse-charge dynamics in electrochemical systems," *Phys. Rev. E*, vol. 70, p. 021506, Jan 2004.

- [25] M. S. Kilic, M. Z. Bazant, and A. Ajdari, “Steric effects in the dynamics of electrolytes at large applied voltages. i. double-layer charging,” *Phys. Rev. E*, vol. 75, p. 021502, Jan 2007.
- [26] P. M. Biesheuvel, B. van Limpt, and A. van der Wal, “Dynamic adsorption/desorption process model for capacitive deionization,” *J Phys Chem C*, vol. 113, pp. 5636–5640, Jan 2009.
- [27] R. B. Schoch, J. Han, and P. Renaud, “Transport phenomena in nanofluidics,” *Rev Mod Phys*, vol. 80, pp. 839–883, Jan 2008.
- [28] R. F. Probstein, *Physicochemical Hydrodynamics: An Introduction*. Hoboken, N.J.: Wiley-Interscience, 2nd ed., 2003.
- [29] M. Z. Bazant, M. S. Kilic, B. D. Storey, and A. Ajdari, “Nonlinear electrokinetics at large voltages,” *New J Phys*, vol. 11, p. 075016, Jan 2009.
- [30] E. Avraham, Y. Bouhadana, A. Soffer, and D. Aurbach, “Limitation of charge efficiency in capacitive deionization,” *J Electrochem Soc*, vol. 156, pp. P95–P99, Jan 2009.
- [31] A. J. Bard and L. R. Faulkner, *Electrochemical methods : fundamentals and applications*. John Wiley, 2nd ed., 2001.
- [32] B. E. Conway, *Electrochemical Supercapacitors: Scientific Fundamentals and Technological Applications*. Kluwer Academic/Plenum Publishers, 1999.
- [33] M. S. Kilic, M. Z. Bazant, and A. Ajdari, “Steric effects in the dynamics of electrolytes at large applied voltages. ii. modified poisson-nernst-planck equations,” *Phys. Rev. E*, vol. 75, p. 021503, Jan 2007.

- [34] J. Chmiola, G. Yushin, Y. Gogotsi, C. Portet, P. Simon, and P. L. Taberna, “Anomalous increase in carbon capacitance at pore sizes less than 1 nanometer,” *Science*, vol. 313, pp. 1760–1763, Jan 2006.
- [35] C. Largeot, C. Portet, J. Chmiola, P.-L. Taberna, Y. Gogotsi, and P. Simon, “Relation between the ion size and pore size for an electric double-layer capacitor,” *J. Am. Chem. Soc.*, vol. 130, pp. 2730–+, Jan 2008.
- [36] R. Lin, P. L. Taberna, J. Chmiola, D. Guay, Y. Gogotsi, and P. Simon, “Microelectrode study of pore size, ion size, and solvent effects on the charge/discharge behavior of microporous carbons for electrical double-layer capacitors,” *J Electrochem Soc*, vol. 156, pp. A7–A12, Jan 2009.
- [37] J. Chmiola, C. Largeot, P.-L. Taberna, P. Simon, and Y. Gogotsi, “Desolvation of ions in subnanometer pores and its effect on capacitance and double-layer theory,” *Angew Chem Int Edit*, vol. 47, pp. 3392–3395, Jan 2008.
- [38] G. L. Athens, R. M. Shayib, and B. F. Chmelka, “Functionalization of mesostructured inorganic–organic and porous inorganic materials,” *Current Opinion in Colloid & Interface Science*, vol. 14, pp. 281–292, Jun 2009.
- [39] M. Bazant, M. Kilic, B. Storey, and A. Ajdari, “Towards an understanding of nonlinear electrokinetics at large applied voltages in concentrated solutions,” *submitted (arXiv: 0903.4790 v1)*, 2009.



# Appendix A

## Literature Review Summary Chart

Author	Date	Journal	Electrode	Electrolyte	Measurement Technique	Time Scale	Concentration Test Param.
Ahn	2005	Mat Sci and Eng	carbon cloth etched in KOH and HNO <sub>3</sub>	0.5 M NaCl	CV, Chronoamp, and flow with conductivity	sec-min	2000 uS/cm and 6000 uS/cm: ~30% decrease in C after 4 min, charged to 1.5 V
Avraham	2009	ECS	carbon cloth (ACC-507-15 from Nippon Kynol) 1440 m <sup>2</sup> /g	0.1 M NaCl	flow with conductivity, also did CV	min	mainly CV changes
Avraham	2007	J Phys Chem	CVD of carbon on ACC to reduce pore size	0.1 M NaCl, CaCl <sub>2</sub> , MgCl <sub>2</sub>	CV	-	
Conway	2001	Elect Acta	carbon felt	H <sub>2</sub> SO <sub>4</sub> (CV), Na-salts	CV, adsorption based on sol'n resistance	min 10s	no NaCl?
Gao	2009	Thin Films	CNT-CNF film on graphite	1 M KCl, 0.0015 M NaCl (conduct)	CV, impedance, conductivity	min 10s	50 us/cm to 43 us/cm after 100 min
Hwang	2003	J NonCryst Sol	carbon aerogel	6 M H <sub>2</sub> SO <sub>4</sub>	pH, CV		just CV and isotherms
Jung	2006	Desalination	carbon aerogel	NaCl	flow with conductivity	hours	100 us/cm to 7.2 us/cm after 15 min at 1.5V (charts)
Lee	2007	Desalination	carbon composite with PTFE	0.5 M NaCl	CV and flow conductance	min-hrs	2000us/cm to 750 us/cm; 1.4 V 80 ml/min
Leonard	2009	Elect Acta	SiO <sub>2</sub> and Mg-Al <sub>2</sub> O <sub>3</sub>	NaCl, FeCl <sub>3</sub> , MnCl <sub>2</sub> , CaCl <sub>2</sub> , etc	zeta potential (electrode), flow with concentration	min	1.5 V; 90% Ca removed in 20 min
Li H	2008	Water Research	CNT-CNF composite film	NaCl	conductivity flow	min 10s	(chart) ACC: 1020-698 us/cm; CNT: 994-684 us/cm; 1.2V
Li L	2009	Carbon	ordered mesoporous carbon	0.1 M NaCl (CV)	CV and flow conductance	min 10s	100us/cm solutions, total amount absorbed 15.9umol/g...different materials
Lim	2008	Desalination	AC with PVDF binder	0.1 M Na <sub>2</sub> SO <sub>4</sub> (CV)	CV		no flow just CV
Noked	2009	J Phys Chem	CVD on ACC	NaCl, NaNO <sub>3</sub>	CV and adsorbed gas		no flow, CV and gas adsorption
Oh	2006	Thin Films	nanoporous carbon cloth	0.5 M NaCl	CV, chronoamp, conductivity	sec-min	1-1.5 V applied, 25 ml/min, 200us/cm-800us/cm
Pan	2009	Desalination	CNT-CNF composite film	NaCl, NaNO <sub>3</sub> , Na <sub>2</sub> SO <sub>4</sub>	CV, impedance, conductivity	sec-min	
Park	2007	Desalination	activated carbon sheet with PTFE binder	0.5 M NaCl	CV and flow conductance	min-hrs	salt removal rate % chart; 0.5 M 1.2V 40 ml/min C/CO <sup>-</sup> 5
Ryoo	2003	J Colloid	ACC and Ti-ACC	NaCl (mM)	CV, Langmuir isotherms, adsorption amount		0.1 mM 1.2V c/c <sup>0</sup> ~0.5 Ti-Acc
Sorenson	1992	J Chem Soc					
Wang XZ	2006	App Phy Let	CNT-CNF composite film	NaCl 100ppm	flow with conductivity	min-hrs	salt removal rate % chart; 1.5 mM 1.2V 40 ml/min
Wang XZ	2006	ECS	CNT-CNF composite film	NaCl	flow with conductivity	min 10s	
Xu	2008	Water Research	carbon aerogel	NaCl with field water	flow with conductivity	min-hrs	
Yang CM	2004	Desalination	carbon aerogel-silica gell	NaCl 1000ppm	step voltage	mins	
Yang KL	2001	Langmuir	carbon aerogel				
Zou	2007	Desalination	activated carbon coated with TiO <sub>2</sub>	500 ppm NaCl	CV and flow with conductivity	min	OMC 50 us/cm-25 us/cm: 11.6 umol/g; ACC 4.3 umol/g
Zou	2008	Water Research	AC and OMC	NaCl 0.1-1 M	CV		

# Appendix B

## Fabrication Process Flow

The process for the platinum liftoff was adapted from Dr. Sung-Jae Kim in the Micro/Nanofluidic BioMEMS Group in RLE. Starting from highly conductive silicon wafers with a layer of thermal oxide:

### *Photolithography*

1. Dehydration at 95C for 3 min
2. For NR71-3000P Spin 750rpm, 6sec, 3000rpm, 40sec
3. Prebake at 130C for 3 min
4. Exposure 30 sec
5. Postbake at 110C for 3.5 min
6. Develop in RD6 for 30 sec
7. Wash and dry

### *Platinum Deposition*

1. Dehydrate for 1 hour
2. Oxygen plasma for 10 minutes
3. Deposit 20 nm of titanium at a rate of  $1\text{\AA}/\text{s}$
4. Deposit 200 nm of platinum at a rate of  $2\text{\AA}/\text{s}$

*Platinum Liftoff*

1. Place wafers in acetone for 24 hours
2. If metal is not completely removed, ultrasonicate for 90 minutes
3. Wash and dry
4. Dice wafers to desired size

# Appendix C

## Matlab Scripts

### C.1 Flow Cell Real-Time Concentration Calculation

```
function cin = get_cin(t,c)
n = length(t);
c0=270; % conductivity of initial inlet stream
Q = 10e-6/60; % flow rate
V0 = 7e-6; % initial fluid volume
V = Q*t+V0; % volume as a function of time
cin(1) = c0;
dt = t(2)-t(1);
% integration to find cin
for i = 2:n
    %cin(i) = c(i)*V(i)/Q/dt-sum(cin(1:i-1));
    cin(i) = c(i)*V(i)/Q/dt-trapz(cin);
end
```

## C.2 Micro Flow Cell Data Analysis

```
%%% Get Data %%%%%%%%%%
%%%%%%%%%%%%%%%%%%%%%%%%%%%%%%%%%%%%%%%%%%%%%%%%%%%%%%%%%%%%%%%%%%%%%%%%
clear all
close all

filename = '1mM4Vflow.csv';
channel= [5, 6];
[acc, data] = dataread(filename, channel);
%%%%%%%%%%%%%%%%%%%%%%%%%%%%%%%%%%%%%%%%%%%%%%%%%%%%%%%%%%%%%%%%%%%%%%%%

%%% Sort Conductivity Readings %%%%%%%%%%
%%%%%%%%%%%%%%%%%%%%%%%%%%%%%%%%%%%%%%%%%%%%%%%%%%%%%%%%%%%%%%%%%%%%%%%%
maxstep = max(data(:,7));
for i = 2:maxstep
    ind = find(data(:,7)==i);
    %sizevector(i-1) = length(ind);
    V(:,i-1) = data(ind,9);
    I(:,i-1) = data(ind,10);
end
%%%%%%%%%%%%%%%%%%%%%%%%%%%%%%%%%%%%%%%%%%%%%%%%%%%%%%%%%%%%%%%%%%%%%%%%

%%%%%%%% Find resistance %%%%%%%%%%
%%%%%%%%%%%%%%%%%%%%%%%%%%%%%%%%%%%%%%%%%%%%%%%%%%%%%%%%%%%%%%%%%%%%%%%%
```

```

n=length(V);
[r,c]=size(V);

for k=1:c
    V1 = V(:,k);
    I1 = I(:,k);
    j = 1;
    for i = 1:n-1
        if sign(V1(i))~= sign(V1(i+1))
            R(j) = abs((V1(i+1)-V1(i))/(I1(i+1)-I1(i)));
            j = j+1;
        end
    end
    end
    Vrms = (sum(V1.*V1)/length(V1)).^.5;
    Irms = (sum(I1.*I1)/length(I1)).^.5;
    Ravg(k) = mean(R);
    Rrms(k) = Vrms/Irms;
    clear R;
end

```